9-1-2015

STRUCTURAL INFLUENCES ON INTENSITY INTERFEROMETRY CORRELATION

Mark Harris

Mark Alan Harris
_____
Candidate

Civil Engineering
_____
Department

This dissertation is approved, and it is acceptable in quality and form for publication:

Approved by the Dissertation Committee:

Dr. Arup Maji , Chairperson
_____

Dr. Timothy Ross
_____

Dr. Rafiqul Tarefder
_____

_____

_____

_____

_____

_____

STRUCTURAL INFLUENCES ON INTENSITY
INTERFEROMETRY CORRELATION

by

MARK A. HARRIS

DISSERTATION

Submitted in Partial Fulfillment of the
Requirements for the Degree of

Doctor of Philosophy
Engineering

The University of New Mexico
Albuquerque, New Mexico

July 2015

DEDICATION

While standing near my poster presentation with my preliminary dissertation results I was told by a collegue "You certainly have grit Mark!". This led me to think of my flaws and how in the end they are always overpowered by my perseverance and positive attitude. So I dedicate this dissertation to all those people who continue to pursue their goals and dreams in the face of adversity and failure. As my father has told me time and time again "Never ever ever ever EVER give up!".

ACKNOWLEDGMENTS

Structural Influences on Intensity Interferometry Correlation

by

MARK HARRIS

B.S., Astrophysics, University of New Mexico, 2002
M.S., Civil Engineering, University of New Mexico, 2008

Ph.D., Engineering, University of New Mexico, 2015

ABSTRACT

Pairing the information received from multiple telescopes to explore the universe is typically based on the interference phenomenon between amplitudes of light, rather their intensities. Brighter sources and larger telescopes allow for greater amounts of light to be collected, but do not specifically involve the intensity interference of electromagnetic fields. There is an alternate form of creating images of distant objects called Intensity Interferometry (II), which is less sensitive to atmospheric distortions and aberrations of telescope surfaces. The deficiencies of II are overcome as photo detectors become more sensitive and computers more powerful. In recognition of this possibility this dissertation investigates how the deformation of a large optical surface would influence the accuracy of II. This research first involved obtaining an understanding of the theoretical foundation of II and statistics (based on quantum mechanics) of photon correlations. Optical Ray-tracing and Finite Element Analyses were thereafter integrated to answer this question: how would the correlation of the intensity field change as a large light weight reflective structure deforms? Analytical models based on the theory of the deformation of shells were developed to validate the Finite Element Analyses. In this study a single focal parabolic reflector of an Intensity Interferometer (II) system is simulated. The extent that dynamic focal properties amongst a parabolic reflector change the statistics of the light at a detector is analyzed. A ray tracing algorithm is used to examine how the statistical variations of simulated monochromatic stellar light changes from the source to the detector. Varying the positions of the detector from the focal plane and the surface profile of the mirror develops a metric to understand how the various scenarios affect the statistics of the

detected light and the correlation measurement between the source and detector. Photon streams are evaluated for light distribution, time of flight, and statistical changes at a detector. This research and analysis are used as a means to develop a tool to quantify how structural perturbations of focal mirrors affect the statistics of photon stream detection's inherent in II instrumentation and science.

Table of Contents

List of Figures

List of Tables

Chapter 1

1) Introduction and Motivation

The primary focus of this research is based on principles of electromagnetic wave mechanics incorporating geometric optics that correlate the light emitted/reflected from an object to that which is observable at an optical sensor. An integral aspect of this research involves the advancement of knowledge in relating the coupling equations of structural mechanics, Intensity Interferometry (II) optics, and photon statistics. The advantage of utilizing II relies on the fact that this technique measures the finite changes in the intensity of a light wave, not the addition of amplitudes as in Amplitude Interferometry (AI). A basic two element setup using II technology measures the square of the modulus of the coherence producing phase terms that average to zero and no image is formed. Measuring the intensities of light waves has significant advantages because it requires less precision involved with the light collecting mechanics and timing correlation techniques. This dissertation work develops a complete analysis system that can be scaled to other models which evaluates the effects of mirror shape perturbations on II technologies. As advancing technology increases detector response time and efficiencies it will become apparent that future generations in optics and telescope design will need to address how distortions in light collectors affect the statistics of photons (narrow bandwidths and short timescales) for II science. A novel algorithm has been developed which combines many distinct software tools and the physics of II into one platform described in-depth throughout this dissertation.

Humanity has been observing the universe since the dawn of time. The original

method incorporated empirical senses such as the eye but has since evolved to view vastly distant objects using state of the art imaging equipment and computational power to visualize and understand our universe. The majority of stellar objects are considered point sources and much information falls beyond what can be obtained by just analyzing spectrums and images. A great wealth of knowledge of the universe is still hidden and is continually being discovered incorporating greater angular resolution imaging techniques. The invention of observational interferometry has played a pivotal role in our ability to observe the universe in significant detail by combining the light gathering power of multiple telescopes integrated into one image. Amplitude Interferometry (AI) began in the radio portion of the electromagnetic spectrum (example: the Very Large Array, near Socorro, NM) where it became apparent that matching phases of the gathered light having spatially separated receivers provides an enhanced resolution of observed objects. In recent years, great efforts have been made to establish AI techniques in the optical portion of the spectrum.

Although AI is the primary multiple receiver instrument coupling techniques astronomers currently use to gather data from the heavens, it is plagued by some fundamental hardships. Optical long baseline amplitude interferometry must overcome complex data measurements, precision in understanding the measurements, limited sampling of data, and low sensitivity as compared to a single detector experiment [1]. The turbulent nature of the earth's atmosphere directly affects the imaging capabilities of terrestrial based telescopes and limits the observations due to very fast and varying phase information [1]. One main driver to alleviate the seeing problem resides in adaptive optics, which compensates for the dynamic nature of the atmosphere. Overcoming the distortions of the atmosphere requires a constant feedback loop incorporating many telescopic instrument subsystems. Each subsystem (light

collectors, delay lines, image sensors, fringe sensors, adaptive optics, focal instruments) of the an optical AI add their own noise to the system and increase the chance for a failure to occur due to the multiplicative effects of errors [1]. Adaptive optics make it possible to adjust the shape of incoming image by adjusting the shape of the reflecting mirrors, thus, making it possible to combine the images of multiple telescopes to obtain a greater resolution and enhanced imaging of observed objects. A second solution to the atmospheric distortion is to place telescopes above the atmosphere, which is expensive and technically challenging due to the development of equipment able to survive rocket launch forces and the extreme conditions of interplanetary space.

A promising technique was discovered that could measure the size of distant objects and overcome the problems of the earth's atmospheric distortions [2] called Intensity Interferometry (II). Intensity Interferometry is a relatively unexplored imaging technique due to its lack of sensitivity compared to historically established amplitude interferometry. The reason AI was employed almost exclusively was due to its established theoretical and documented development [3]. The sensitivity of II technology can be increased by redundant baselines operating in multiple narrow bandwidth channels and by increasing the electrical bandwidth [4]. II has its inherent limitations, as well as some very significant advantages and science avenues that have yet to be explored in depth. II combines statistical photonic information or the intensities of electromagnetic waves between two or more detectors. II has been used in many areas besides astronomy including the world of subatomic particle physics [5]. The discovery of the II optical phenomenon was largely due to the efforts of Robert Hanbury Brown and began quantum optics [2]. The true confirmation of this imaging technique was established in the radio portion of the spectrum conducted with solar light in 1950 by Hanbury Brown, and Twiss [2]. Eventually, Hanbury Brown and Twiss

3

built an II instrument that operated in the optical portion of the electromagnetic spectrum. They used various mathematical algorithms with their observational measurements to extrapolate the angular diameter of many bright stars. II based instruments are relatively new to the scientific community and have much room for development. II techniques are constantly being developed and inevitably becoming an asset for the observational and surveillance communities.

AI has been used as an imaging device especially for distant astrophysical objects. The original images incorporated photosensitive materials such as film and glass plates, but has since evolved to use charge coupling devices (CCD's) which convert photons into electrons and ultimately stored as digital bits. Computers can now store images of astrophysics in many parts of the electromagnetic spectrum for further processing. The "images" first obtained by an II instrument were not classic images but more of a correlation profile that was later interpreted as an angular extent of the object. The first II instruments used only two receivers measuring in real time with one baseline, thereby losing the phase information necessary to reconstruct a 2-dimensional image. The imaging capabilities of an II must employ more than two receivers to recover the phase of the incoming light. Multi-detector II systems incorporating three or more receivers can extrapolate 2-dimensional coordinate information from a source. This style interferometry can be developed even further to a four detector system that can determine three dimensional coordinates of several sources [6]. Sensitivity and signal to noise ratio's (S/N) are fundamental to most scientific measurements. AI has the advantage of using broadband detectors that use a larger portion of the electromagnetic spectrum at the cost of needing to combine the interferometric information instantaneously. II instruments have the capability to digitally store photonic information and redundant post-processing with a greater precision than AI.

Algorithms have been envisioned to use the stored II data streams coming from uniform linear detector arrays that have a high degree of redundancy which can increase the sensitivity 100-fold [7]. Many multi-telescope arrays already exist for use in high energy astrophysics, detecting Cherenkov radiation (energetic particles entering the atmosphere), and can be changed to operate as II instruments. Changing the mode at which these instruments operate has been the subject of many recent proposals and Ph.D. dissertation topics [8].

Many additional aspects of II technology have also been researched in great detail such as the geometrical arrangement of II receivers [9], space-based intensity interferometry [10], II to detect satellites [11], and comparison of older II technologies to current II trends [12]. Recent advances in data acquisition, processing, and photonics, along with position sensing and control of structures with exceedingly large baselines (greater resolution) have opened the door for utilizing the unique characteristics of II for plasma physics [13] and medical imaging [14]. Current publications imply even more applications for II including detecting Exo-planets [15], imaging hot stars at very high resolutions [8], general micro-arcsec imaging from the ground [16], and astrophysics in the ultra-short timescales [17]. The actual measurement is based on rapid photon-counting detectors with fast digital signal processors and computations of different statistical functions of the photon arrival times.

In addition to the errors that arise from light being distorted on its way to instruments on earth, both AI and II observing instruments use light collectors and photo-electronics that introduce errors themselves. Materials and hardware that are designed to convert photons into storable digital bits introduce thermal noise and electron charge transfer deficiencies. With regards to distortions on reflective mirror surfaces, errors are introduced due to imperfections in the reflecting surface on the

microscopic scale, as well as, larger scale deformations which form non-perfect images at the focal plane. These aberrations are well understood for AI, but have not been fully analyzed for II systems and instrumentation. *Understanding the statistical nature of the photons received at a detector due to perturbations from a perfect parabolic afocal (single surface reflection) reflecting mirrored surface is the prime objective of this dissertation research.*

Chapter 2

2) Intensity Interferometry

An intensity interferometer combines light signals from two or more telescopes that are simultaneously measuring the random and very rapid [quantum] fluctuations in the intensity of light from some particular star [18] or other thermal object of interest. In essence natural thermal light sources are never monochromatic in nature, but instead are observed to have a bandwidth even with the most accurate filters. This finite bandwidth of light allows multiple frequency components to interfere with each other giving rise to beat frequencies in the light intensities. These beat frequencies can be orders of magnitude lower than the frequency of the light itself. The correlation between the intensity of light at the two telescopes decreases gradually as the two telescopes are moved further apart and the rate at which the correlation drops is used to measure the angular size of a given source. The correlation itself is a function of photon statistics (coherence, bandwidth, intensity, etc.) to be discussed later. While the coherence (related to correlation of the intensities) is highest while the telescopes are close together, determining its value requires long duration of data collection to minimize the effect of various noise sources.

The origins of Intensity Interferometry (II) started with the measurement of the diameter of the sun by Hanbury Brown and Twiss in 1950 using two radio telescopes [2]. Being a radio astronomer Hanbury Brown (1949) had a realization that "if the radiation received at two places is mutually coherent, then the fluctuation in the intensity of the signals received at those two places is mutually coherent" [19]. Essentially, the low frequency intensity oscillations are correlated. Hanbury Brown eventually brought on Richard Twiss, who had the mathematical training to apply the

mathematical theory to the analysis of intensity correlations. They demonstrated that it is possible to go beyond the conventions in Amplitude Interferometry (AI) by analyzing the intensity, spectral characteristics, and polarization of light sources of the first order correlation and access the information contained in a higher order regimes.

II is in essence the Hanbury Brown and Twiss effect (HBT) and differs from AI, or the interference of electromagnetic fields, in that II measures the second order correlation of light intensities known as photon counting, or the recording of the time histories of photodetector signals. II and its enhanced resolution capabilities are also used in the detection of subatomic particles in high energy experiments which require precision with extremely small diameters [5, 13]. The initial HBT experiment used two crude optical telescopes that incorporated the newly developed II technique. It became evident to use more than two receivers so that phase information can be obtained to form an image. The original two telescope instrument was used to measure the rapid and random fluctuations in the intensity of light from a blackbody such as a star, to obtain an angular extent or size of the observed object. The measurement is made when the two telescopes are placed close together, both measuring the same signal, then they are moved apart and the observed fluctuations gradually vary and become de-correlated: How rapidly this happens gives a measure of the spatial coherence of the stars light and the angular extent of the star [20]. Measurements taken from the original HBT experiment plotted correlation values between the two photomultiplier detectors and various detector separations as in Figure 2.1. The point where the correlation value equals zero defines that angular extend of the source and will be discussed in depth in Chapter 5.
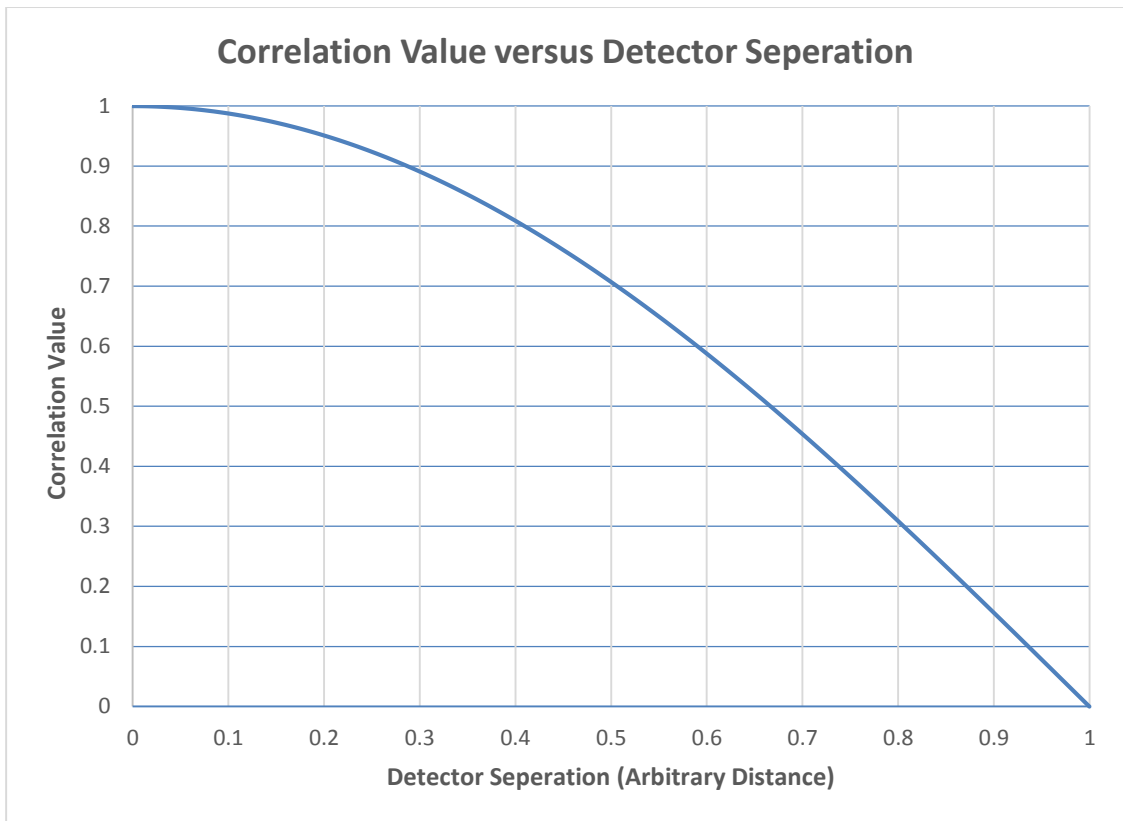
Figure 2.1 - Correlation Values Versus Detector Separation

2.1 History of II

The first radio intensity interferometer was the result of Hanbury Brown's deep contemplation that occurred late one evening in 1949. He wanted to discover a better way of gaining greater precision on the angular extent of stars. He wondered how far apart the receivers should be located to get the best resolution while working in the radio part of the spectrum. At the time, the farthest physical distances to separate two detectors and observe in real time would be on opposite sides of the planet. He imagined the difficulties there would be in how to produce a coherent oscillator for those two points. Then he had an epiphany that the coherent oscillator might not be necessary in the first place. Hanbury Brown convinced himself with the following thought experiment [2]:

"As an example, I imagined a simple detector which demodulated waves from the source and displayed them and the usual noise which one sees on a cathode-ray oscilloscope. If one could take simultaneous photographs of the noise at two stations, would the two pictures look the same? This question led directly to the idea of the correlation of intensity fluctuations and to the principle of intensity interferometry."

Then with the mathematical expertise of Richard Twiss, a plan was formulated to support the hypothesis with a formal derivation of the phenomenon and an actual experiment. With the help of R. C. Jennisona, an intensity interferometer utilizing two radio antenna was constructed. This first experiment was directed at the sun observing at a frequency of 125 MHz and from a correlation measurement the theory was finally confirmed. Later, measurements of the two brightest known radio sources, Cygnus A and Cassiopeia A, were also confirmed for their respective diameters with the help of M.K. Das

Gupta. Later the stellar diameter measurements were confirmed with amplitude interferometers in Cambridge and Sydney [2].

Additional research was conducted to devise the first optical intensity interferometer. Traditionally, radio engineers thought radio light to consist of many photons with very little energy and, therefore, the wave nature of their detection was a fundamental design parameter (aerial antennae). When Hanbury Brown and Twiss began to brainstorm on how to build an intensity interferometer in the optical portion of the spectrum it was apparent to them that they needed to incorporate a new photon detection system. By exploiting the fact that optical photons possess greater energy and are less numerous than radio photons coming from the sky, the original optical interferometer was built with a parabolic concentrator focusing on a single detector (photomultiplier tube), much like a radio dish concentrates to an aerial array. This design led to the discovery that it was not necessary to have much precision in the optical reflectors surface error because imaging was no longer important in this style of telescope.

The first optical interferometer was set up in a dark room, at Jodrell Bank, Australia. An artificial star was formed with a mercury arc light emission focused on a pin hole. The light coming from the pin hole was divided into two beams in order to illuminate two photomultipliers which would be spatially separated to introduce the variations necessary in an interferometer setup. Intensity correlations were measured at various detector separations confirming the II theory and eventually published in January of 1956 [2].

The initial large scale intensity interferometer was built from 1962-1964 in Narrabri, Australia. The instrument had an interesting and unconventional design with two

large reflectors on two trucks situated on railroad tracks arranged in a circle 188 meters in diameter. Cables connected the trucks to the main tower where the electrical information would be assessed (Figure 2.2) [2]. The parabolic reflectors were 6.5 meters in diameter with the phototube receivers at the end of 11 meter steel tubing and were mounted with the ability to move in three different orientations. Each reflector consisted of 252 hexagonal mirrors with focal lengths of 11 meters and a field of view in the sky of about 8'x8' (arcseconds). The cathodes of the photomultiplier tubes had a quantum efficiency of 20% at a wavelength of 4400 Angstroms with an anode current of 100 μA. The fluctuations of the D.C. signals in the two different channels were combined in a unidirectional output.
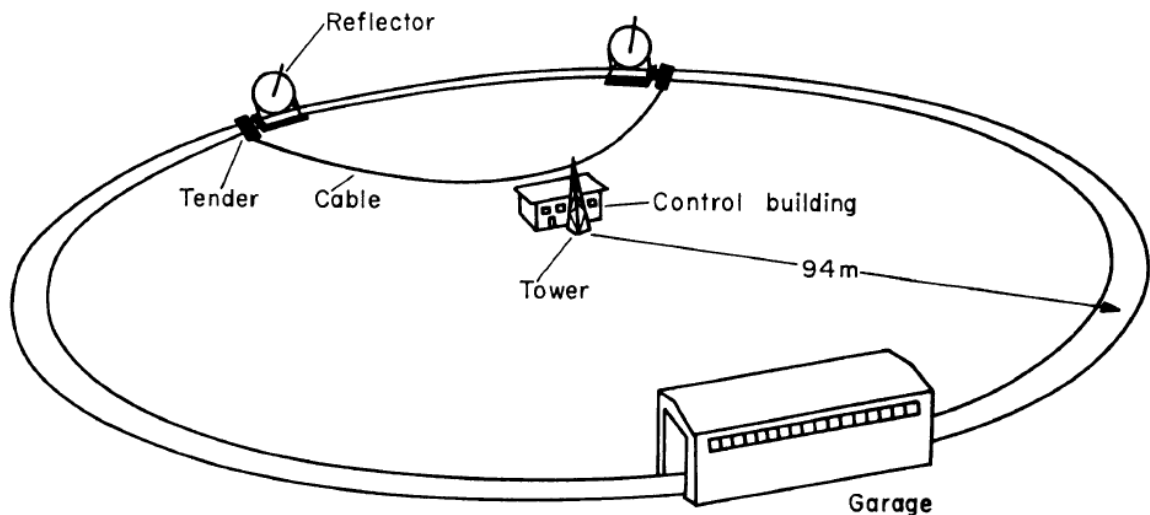
Figure 2.2 - Large Optical II Telescope System [2]

This circular arrangement of the detectors allows for a consistent baseline perpendicular to the observed stellar source. They used this instrument to measure the angular diameter of 32 of the nearest and brightest stars [2].

2.2 Theory of Coherent Light

To begin the discussion of interference, it's necessary to start with the definition of coherence. A primary example is observing the deviations of a distant point source of light and from that source extrapolate information that is not point-like. Interference phenomenon incorporated in a plane wave representation (ignoring polarization) of light can be described as two forms of coherence. Spatial coherence is light whose frequency and phase are the same in all space. Temporal coherence is a description in which the lights frequency and phase are known for the complete observational time. Spatial and temporal coherence are the ideal case for observing interference.

The classical wave nature description of coherence, begins with the superposition of many monochromatic plane waves that produce an amplitude of on electric field, E(t), of light at a fixed position [21]:

$$E(t) = \int E(\omega)e^{iwt}d\omega \qquad [\text{Eq. 2.1}]$$

An electric field with nominal frequency, ω, will have some value during a time interval Δt giving a $E(\omega)$ changing in time over a given bandwidth $\Delta \omega$. Beat frequencies of the monochromatic light are the values that vary as $2\pi/\Delta w$ and individual frequencies within the intensity of an electric field are values of $2\pi/W_o$ where W_o, is the central frequency (Figure 2.3).
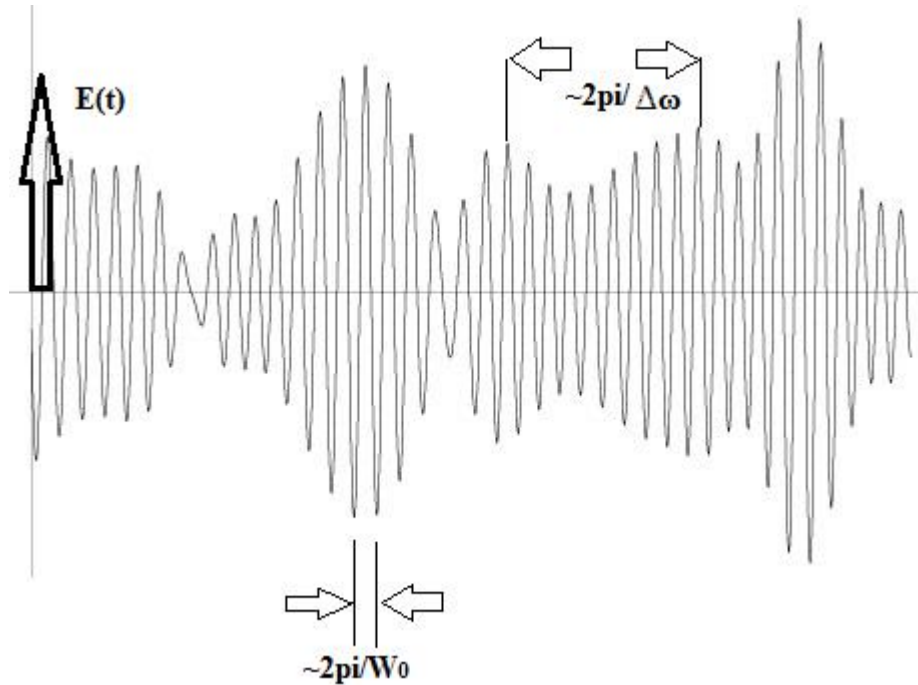
Figure 2.3 - Vibrations for Quasi-Monochromatic Light

2.3 Coherence Time and Length

An electric field E(t) has some non-zero amplitude varying value in the time interval observed Δt. The Δw is the bandwidth which is described as $e^{iw\Delta t}$ of Equation 2.1, which happen when Δw is approximately equal to the reciprocal of Δt:

$$\Delta t \leq \frac{2\pi}{\Delta\omega} \qquad [\text{Eq. 2.2}]$$

Defining a coherence time, Δt, is the where light is considered to have a known phase and be considered monochromatic in nature. The length of this time related to the speed of light is known as the coherence length of light:

14

$$\Delta l = \frac{2\pi c}{\Delta \omega} = \left[\frac{\overline{\lambda}}{\Delta \lambda}\right] \overline{\lambda} \qquad \text{[Eq. 2.3]}$$

Where $\overline{\lambda}$ is the mean wavelength of light and $\Delta \lambda$ effective wavelength range. Spatial coherence and the coherence area can be illustrated and described further with the Young's interference experiment in Figure 2.4. Again, with a monochromatic thermal light source passing through two slits in a screen, Q_1 and Q_2, where the subtended angle between the slits is 2 x $\Delta\theta$. The light interferes on the plane β, where the composition of the interference pattern is the result of the superposition of light intensities from the differing sources. The interference fringe will have a specific value at the axial point, P_o from the sources as long as the following is satisfied [22]:

$$\Delta x \Delta\theta < \overline{\lambda} \qquad \text{[Eq. 2.4]}$$
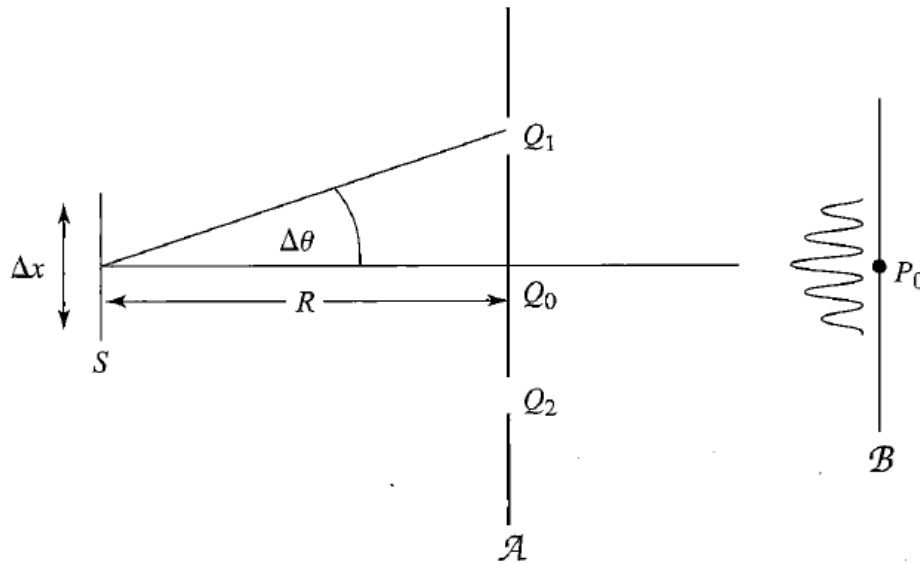
Figure 2.4 - Double Slit Experiment

The coherence time and length are important parameters for the source description. For an II correlation measurement to be accurate the arrival time for a given set of photon streams coming from the same source must be evaluated to on the order of the coherence time. If this condition is not satisfied, than the correlation value is minimized and would be like comparing two random photon streams with the same mean.

2.4 Statistics of Naturally Emitted Photons

The primary information being evaluated is the rate at which thermal light (particle nature of photons) is being received at a detector plane. Many natural phenomenon such as the amount of eggs laid by a group of chickens on any given day [23] or in particular to this research the thermal photon emission process [2] can be described by the Poission distribution. Referencing monochromatic thermal light with a very narrow bandwidth is typically modeled as a Poisson distribution of the number of photons emitted by a source per unit time [2]. The statistics of the Poissonian distribution can be defined as a probability distribution [23]:

$$P(n) = \frac{\lambda^n e^{-\lambda}}{n!} \qquad \text{[Eq. 2.5]}$$

Where P(n) is the probability of finding a given amount of photons with a certain sample time. The value of *n* is the mean value of photons in time and $\lambda = Np$, where N is the number of trials multiplied and p is the probability of *n* occurrences.

There is a large amount of research involving the statistics of photons including accuracy of detection. It was thought all photons had an unpredictable nature with respect to the statistics of detection until the laser was invented. With the onset of quantum mechanics, it was realized that the statistics of photon emission and detection from various sources had a probability distribution associated with them. The probability distribution of intensity fluctuations from thermal sources such as stars are primarily due to the collisions of atoms in the emitting plasma. A large ensemble of emitting atoms from a source also contributes to the statistical nature of emitted light. This chaotic emission of photons creates a "bunching" of photons, meaning they are received in groups at a detector. A correlation (or similarity metric) measurement of the bunching of light from two detectors is the primary metric of II.

2.5 Photon Statistics

Photon flux is a primary driver for making observations and performing scientific analysis of light. The physics involved with photon emission is a necessary starting point in understanding the statistics of photon detection. The light we observe from a thermal source is a statistical process in a macroscopic system. Photon streams are the collection of a group of photons in time. For a specific source the most accurate way to quantify the brightness of the light is by the mean number of photons detected in a given interval of time. However, if another measurement is made within the same time interval from the same source, the mean of photon counts will typically be of a different value. Photons that are emitted from a natural thermal source possess a mathematical distribution between

arrival times. When observing from a macro perspective the arrival times of photons are bunched in a time varying nature as in Figure 2.5 [24]:
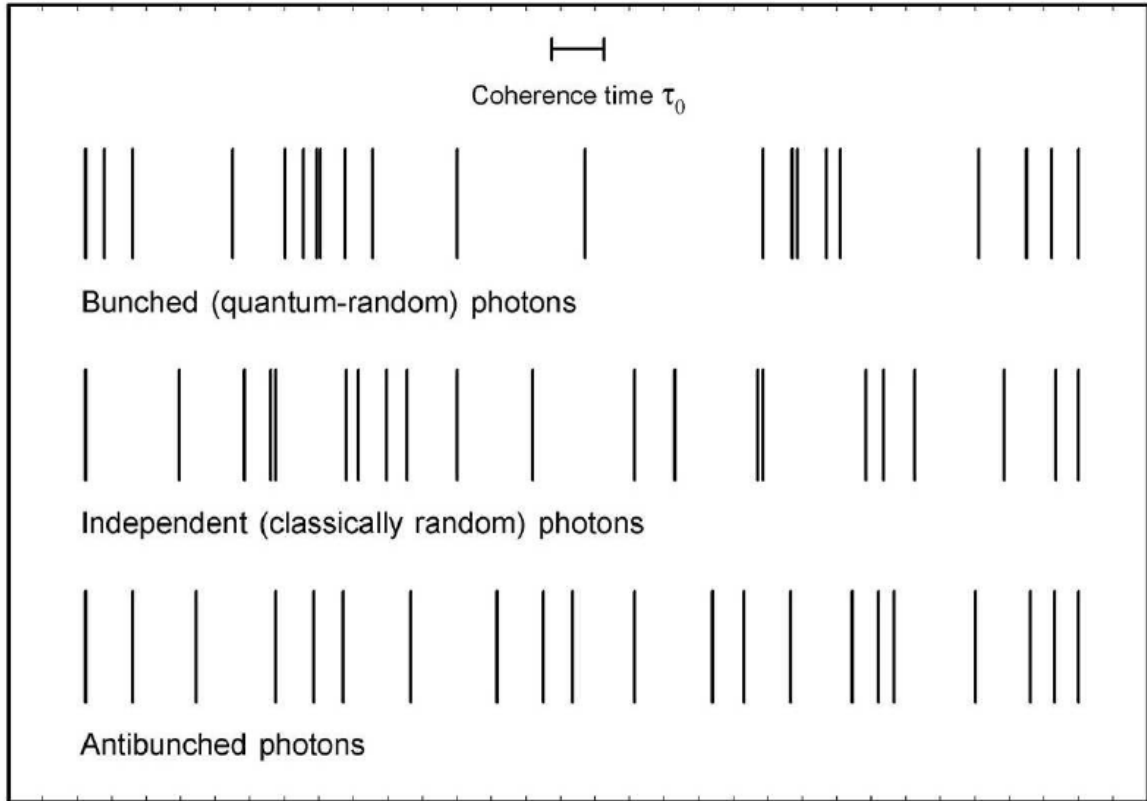
Figure 2.5 - Photon Arrival Time Characteristics

The level of irradiance of a given source must be evaluated and instrumentation components need to be carefully calibrated for accurate observation (Table 2.1) [24]. Photodetectors that are illuminated with an overabundance of light will be overwhelmed with noise and the signal will be minimized. Alternatively, observing a source without capturing enough light requires large integration times and introduces the potential that no useful information can be extrapolated.

Source	Mean Photon – Flux Density (photons/s-cm^2)
Starlight	10^6
Moonlight	10^8
Twilight	10^{10}
Indoor light	10^{12}
Sunlight	10^{14}
Laser Light (10-mW He-Ne)	10^{22}

Table 2.1 - Mean Photon Flux per Source

A blackbody degeneracy parameter describes the mean of photon arrival times and is used as the basis for the simulation runs. The mean of photons is defined by the following formula [25]:

$$\bar{n} = \frac{1}{e^{\left(\frac{h\upsilon}{KbT}\right)-1}} \qquad \text{[Eq. 2.6]}$$

Where h is Planks constant, υ frequency of light, K_b is Boltzmann's constant, and T is temperature of the source. Values used for the simulation centered around a wavelength (λ) of 500nm, which equates to a value of 6 x 10^{14} Hz (υ) for the frequency. The temperature of the simulated stellar source was a star with a surface temperature of 2.6 x 10^4 K. These values give a mean, otherwise known as the degeneracy parameter, solving Equation 2.6 with the values from above gives $\bar{n}$ =0.5.

2.6 Photon Stream Correlations

A simplification of the II phenomenon can be developed when using a basic physical explanation. If the light is treated as a particle it can be described as a stream of photons detected in a finite time interval. Assuming that all photons are converted directly to digital bids encoded with an arrival time eliminates the need to add the complexity of intensity fluctuations, detector efficiency, electronic noise, and light loses due to reflections. This theoretical assumption simplifies the noise and signal losses so that integration time can be shortened to time frames manageable by current simulation algorithms and limited computational power.

Due to the chaotic nature of thermal photon emissions, photons tend to arrive in bunches. Measuring a stream of blackbody photons in a very narrow bandwidth gives rise to their arrival times being far apart from each other. This phenomenon is described in more detail in section 2.10. The detector time response is far greater than the time between photons, thus, a quantum interpretation of the light can be used (discrete wave packets of energy). When observing weak power emissions the light in question is assumed to be quasi-monochromatic implying that the effective bandwidth, $\triangle\omega$, is much smaller than its mean frequency, $\bar{\omega}$ [22].

$$\triangle\omega \, / \, \bar{\omega} << 1 \qquad\qquad \text{[Eq. 2.7]}$$

So the second-order correlation function can be written1 as [26]:

$$g^{(2)} = \frac{<n1(t)n2(t)>}{<n1(t)><n2(t)>} \qquad\qquad \text{[Eq. 2.8]}$$

Where n1 and n2 are the numbers of photons counted in a certain time interval for each detector. The second order correlation measurement is used as the primary metric for this dissertations analysis. The brackets indicate an average, where the numerator is the average of the product and the denominator is the product of the average. Photon counting detectors of two beams of light and employing the second order correlation function gives the intensity correlation. For quantum optics, using the second order correlation function can be used to identify the state of the photon streams (Figure 2.5). Anti-bunched photons are used for communications, while bunched photons are the primary information source for II. If the photon streams from multiple II instruments are measured with enough accuracy, the delay between the photon streams can be assessed as well as phase information [27].

2.7 Detectors and Correlators

Recent and developing technologies are opening new avenues of research related to observing natural radiative phenomenon on the shortest of timescales. The detection of light is a process that is bound by physics (uncertainty principle), materials, photoelectric design, and computational speeds. Photon detection is statistical in nature and all the instrumental components play a specific role in the precision and accuracy of a given measurement. Technologies of the 1960's for photon counting and time correlated counting techniques used photomultiplier tubes (vacuum tube detectors with high internal gain). Current single photon avalanche diodes (SPAD) can produce photon timing resolution of 10 picoseconds (10^{-12} sec). Silicon based SPAD devices are constantly being

improved. They incorporate breakthrough technologies, have high quantum efficiencies, and are manufactured at a low cost [28].

Additionally, a major push is being conducted in the astrophysics community to move to higher spatial and temporal resolutions. Traditional means of obtaining digital information form astrophysical sources incorporates charge couple device (CCD's) detectors with current readout rates ranges between 1-10 milliseconds. CCD photon detection technology designs are limited in speeds and charge transfer efficiencies, rendering them inadequate for II and quantum optics. The Overwhelmingly Large Telescope of the European Southern Observatory is proposing an instrument called QuantEYE that is designed for sub-nanosecond time resolutions, as well as, Ghz photon count rates. This in an effort to study timescales sufficiently short to unveil the quantum optical nature and statistics of photon arrival times from astrophysical sources. Some of the important information sought after is if a given photon stream may carry information about how it was created and modified by its propagation to a detector [29].

2.8 Simulating Intensity Interferometry

Many II simulations and experiments have been performed with varying results. Amongst these, was a computational simulation mixed with a physical experiment that used laser light and artificially simulated chaotic light. By reflecting the laser light in a fluid with independent radiators researchers were able to derive the photon time arrival statistics needed to produce an II effect [30]. Also, simulations representing photons as particles that do not include quantum mechanics, wave theory, or probability theory have

22

been able to reproduce II or the Hanbury Brown-Twiss effect [31]. Photon level Monte-Carlo simulations of II have also been performed to optimize optimal observing configurations and conditions [32].

Studies to determine the most efficient arrangement of multi-telescope II ensembles have also been conducted. It had been determined through some mathematical simulating that a V-shaped pattern provided the best arrangement for maximizing efficiency and relative ease of access for dish maintenance and movement [9]. Further experiments have been conducted with three-telescope configurations where correlation measurements were recorded. These experiments were conducted in order to study the potential for large separation, high resolution, and multi-telescope operation. This research eventually converged to the second order correlation measurement by increasing the observational time from 10 microseconds to 10 seconds [33].

II physics has also been incorporated into some forward modeling techniques that have reconstructed images using Fourier analysis measurements. Forward modeling uses mathematical relations that compare perfect conditions of the observed object, sensors, and environmental conditions to that of the actual measurement [34]. Other simulation algorithms simply use theoretical constructs and some basic assumptions to compare both the classical and quantum photon statistics correlations. M. Facao, A. Lopes, A. L. Silva, and P. Silva produced a mathematical simulation to obtain second order correlation profiles based on equations developed by Hanbury Brown and Twiss [26]. Their paper was elegantly simple and has been adapted to serve as much of the frame work for this dissertation research.

With advancement in the speed of detectors and computation the importance of changes in a reflector shape will become of pivotal importance for advancing the future of II. It has already become evident to many researchers that the increasing efficiency and detector speed will increase the requirement for surface isochronicity of the mirrors [18]. As in AI, path length differences in two different photon counting II instruments can have significant restraints on the mechanical system, especially at longer baselines and space-based II systems [35]. Research has also been performed on various boundary conditions and gravitational loading on parabolic reflectors with results that elude to how forces can cause substantial distortions to a reflector surface [36].

In conclusion, much of the past and current research of II focuses on experimental techniques and increasing signal to noise ratios. Addressing errors introduced from the mechanics and structural aspects of the light collectors involved in II measurements has not been significantly acknowledged. This dissertation research will evolve the key aspects and algorithms used to quantify the significance of how structural deformation can affect II science and be used as a platform for future research and simulations.

Chapter 3

3) Modeling Optics and Reflecting Structures

This research simulates how the shape of an II reflector affects the statistics of light being measured. All mirrors and lenses have some degree of imperfections and surface error. The significance of these flaws has been extensively and historically studied for AI but not for II systems [37]. Of particular importance regarding research on the shape of the light collectors was the original II at Narrabri, Australia depicted in Figure 2.2. The original instrument consisted of 256 mirrors on each reflector, all of which had to be aligned by putting a lamp at the focal point and examining the image at a far way point. Once the mirrors were aligned, Hanbury Brown and Twiss placed a camera at the focal point and followed Jupiter as it rose in the sky. To their disappointment the image varied greatly with elevation. Ultimately, the problem was linked to the bending of the tubing that makes up the larger steel structure dish shape and mirror mounts [2]. However, the changing shape of an II reflector has yet to be examined for its effect on the II measurement.

3.1 Experimental Setup of an II System

The research conducted for this dissertation integrates the laws of geometric optics, mirror mechanics, and the combination of multiple engineering software platforms. A parabolic reflector model was incorporated as it had been used in previous II experiments [2]. The parabolic reflector used in the simulation was based off the reflective dishes used

by Hanbury Brown and Twiss for the original optical II telescope system. A flow diagram
of the simulation variables and algorithm are described in Figure 3.1.
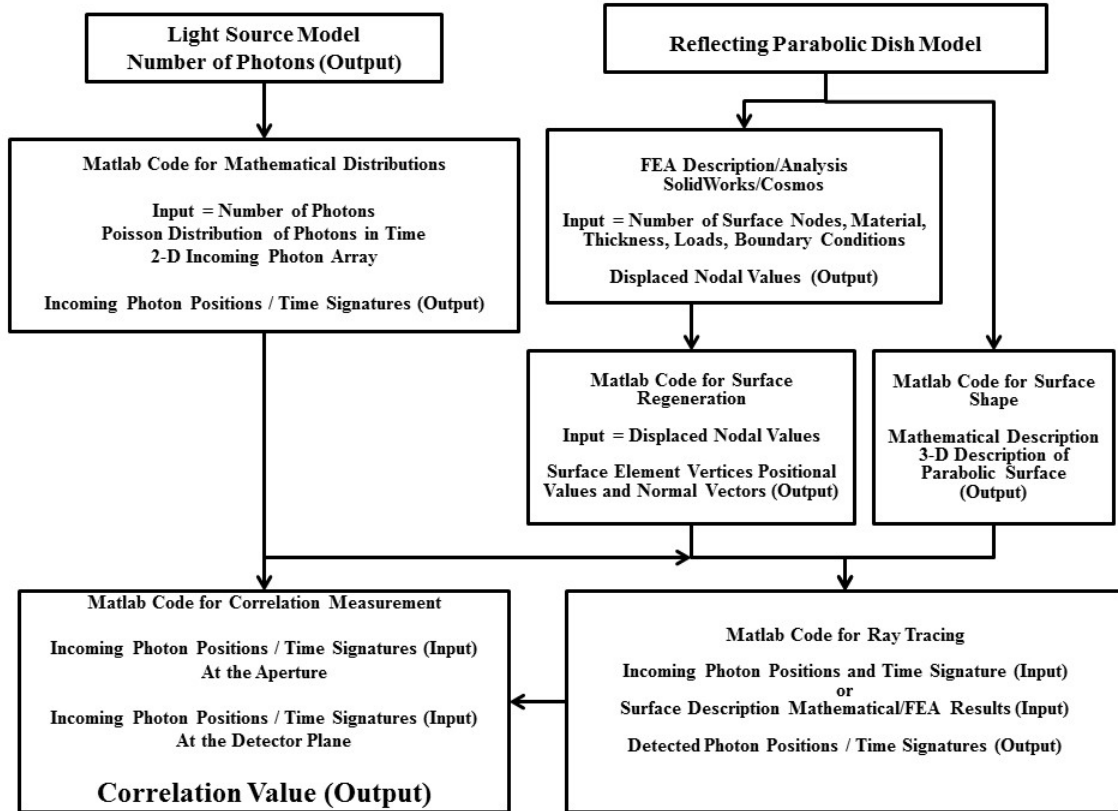
Figure 3.1 – II Simulation Flow Diagram

A functioning parabolic reflector II instrument would encompass many physical
variables such as the observed light source, reflector surface material, detector type, etc.,
which are beyond the scope of this dissertation. The model that is addressed in this research
does not include diffraction effects, reflection losses, detector efficiency loses, or photon
flux loses due to the detector blocking some of the light entering the system from its distant
source as in a focal system. All photons that enter the aperture of the system are recorded
at the focal plane. The objective is to quantify how parabolic mirror distortions affect the

correlation measurements of an II instrument and how the timing of photon statistics change with the introduction of mirror distortions.

Beginning with a simulation algorithm written in Matlab, a preliminary geometric ray tracing code was verified based on mathematical definitions. The original results made physical sense as for the perfect parabolic surface having all photons travelling the same path length (section 5.7), thus confirming mathematically the framework for developing a more sophisticated analysis. A coupling was established between the path length change for a given photon due to a reflection off the perturbed parabolic surface. Distorted surfaces were produced by varying the shape of the reflector mathematically. Further incorporation of more realistic scenarios can be carried out to perform additional research that can be applied to future scientific pursuits and analysis.

A simulation test matrix was developed to formalize the comparative study. An earth based parabolic reflector was subjected to gravitational loading. The parabola dish was simulated to have varying thickness in order to exemplify its effect on the structure that was modeled as a membrane with minimal bending stiffness. Incoming photon statistics and their associated time stamps were compared to that which were impinging on the focal plane after reflecting through the telescope system. This provides a direct comparison to evaluate the effect of parabolic shape perturbations to an II instrument measurement.

3.2 Conceptual Modeling of the Physical System

The model was designed to mimic a single dish of a II multi-telescope system observing a distant thermal source. Most point sources in astronomy are considered to have all radiation coming in parallel to the focal axis of a telescope. Hence the angle between the focal axis and the incoming photon rays are extremely small ($\sin \theta \cong \theta$). The test matrix consisted of a set photons streams reflected off of both unperturbed and distorted parabolic surfaces for comparison. The parabolic surface is modeled to have a surface that reflects all light, like a mirror without any scattering due to microscopic irregularities. As will be discussed in depth in Chapter 5, the parabolic surface is actually made of an ensemble of triangular flat surfaces. A convergence study was performed to describe the limit at which the refinement level of surface elements became acceptable. The photons in the simulation reflect off a specific surface element, eventually impinging on focal plane in which they are recorded.

3.3 Mathematical Modeling of the Conceptual Model

The source of photons can be thought of as a stream of energetic particles travelling at the speed of light. The transition of treating light classically (light wave) to that of describing light as a "quanta" or specific unit of energy (photon) needed to be defined to address light as a particle. This idea of finite energy packets began modern physics and quantum mechanics. A given thermal blackbody source emits polychromatic photons with a large bandwidth of frequencies. With the assumption that an extremely narrow filter can produce monochromatic light it is possible to count the individual photons and produce a

time signature for each. The timing signature of photon arrival times has a Poissonian distribution which is based on the Bose-Einstein photon emission processes in thermal gases as described in section 2.5. A mathematical description on the nature of photon statistics will be elaborated on further in section 5.6.

The geometry of the parabolic reflector is built up from a 2-dimensional to a 3-dimension mathematical model for the simulation algorithm. A perfect parabolic mirror has a unique property of focusing all rays from distant sources to a single focal point which is not very practical for observation of extended sources because an image is not formed. Even though an image is not formed, redundant II arrays and high speed photon detectors can extract phase information to reconstruct images digitally. For scientific purposes, the impinging photons need to be converted to electrons which are stored for future analysis as digital bits. The single focal point allows for unique photoelectronic detectors such as photo multiplier tubes and avalanche diodes to be incorporated. Recent advances in this style of devices are being developed that have extremely high quantum efficiencies and fast read out rates [29]. Higher order measurements with intensity interferometry are increasing the precision of quantum optics and unlocking the knowledge contained in smallest and grandest of scales of our universe [35].

Current methods of modeling physical structures involves computational algorithms encompassing the realm of finite element analysis (FEA). FEA applied to this dissertation focuses on applying a mesh of elements to the complex geometry of the parabolic reflector with a given thickness representing the underlying physics of the simulation setup. The mesh was refined with a high enough density to not only converge on the analytical solution, but also to accurately represent the geometric optics of the ray

tracing algorithm as will be seen in Chapter 5. A plastic material was chosen due to its low material cost, isotropic properties, and small modulus of elasticity compared to metals. The goal in choosing the material was to allow a significant displacement due to a gravitational loading and still be able to extrapolate some of the pertinent physics in the time frames associated with the photon ray travel times. Fixed axial and rotation boundary conditions were applied to the outer rim of the model, forcing all incoming rays through the reflector model. Meaning the modeled incoming light rays would not miss the reflecting parabolic surface. A gravity body force was chosen as the loading scenario to represent an earth based system pointing at sources in the sky. The power of the simulation algorithm proposed is that it can be scaled to any size and a variety of structural characteristics. Many loading and boundary conditions could also be applied for further analysis, although that is beyond the scope of this dissertation.

3.4 Discretization and Algorithm Selection for the Mathematical Model

The discretization and mathematical algorithm selection for the simulation model was based on physical and assumed factors in order to address 'how do structural deformations influence the photon statistics in an Intensity Interferometry telescope?' Thus, the simulation was optimized to fully describe and answer the for mentioned thesis question. With the significant amount of past simulations and experiments involving II, none have fully addressed this question. The results and conclusions of this dissertation work facilitates future researchers to employ the II simulation algorithm incorporating various physical parameters.

Drafting of the physical model began with understanding the parameters of a 2-dimensional parabola as described in section 5.3. Solving the basic equation for the parabolic dish modeled in this research involved drafting an equation driven parabolic curve (with thickness) which was then rotated about an axis of revolution making up a parabolic 3-dimensional object. The subsequent parabolic reflector model was then free to have material properties, loads, and boundary conditions applied to it. The density of the mesh was determined in a two-fold process:

1) The necessity to accurately match the analytical solution involving deformation of a surface of revolution.
2) The requirement that the ray tracing algorithm would complete in a reasonable amount of time (photon number versus triangulated surface number ~computational time).

As with most mechanical systems modeled with computers, a mathematical solver is built into the software to find solutions for various parameters such as stress and displacement. An analytical solution for a surface of revolution is derived with the same boundary conditions and loads as in the FEA model for comparison. A comparison based on maximum displacement verified that the FEA model converged on the analytical solution.

Knowing that the FEA analysis was accurately representing a physical system it was necessary to bring the nodal displacement values into the ray tracing algorithm. Over many iterations and solutions it became possible to extract the specific nodal positional values from the surface of the reflecting parabola as compared to all of the nodes defining the full 3-dimensional object. After a significant amount of research, it was discovered

that it was possible to extract the displaced values of each node and was a major breakthrough for this dissertations' progress. These displaced values $(\Delta x, \Delta y, \Delta z)$ were then added to the original nodal position values to get the subsequent deformed nodal positions.

Once the deformed nodal values were obtained from the FEA analysis it was then necessary to rebuild the reflecting surface from the "nodal cloud" of data points. Using a surface triangulation mathematical algorithm, a complete surface was established with interwoven triangular surfaces meeting at the vertices of the nodal coordinates from the FEA results. The resurfacing algorithm also gave the normal vector out of the plane of each individual triangular surface necessary for the ray tracing algorithm.

3.5 Computer Programming of the Model Simulation

The primary goal of the computer simulations is to model nature as accurately as possible. For this dissertation that meant modeling without introducing non-linear phenomenon, such as thermal noise, as in a typical photodetector. Because this thesis is based on an II telescope, geometric optics, and signal correlations, photon distribution parameters need to be established. As mentioned previously the frequency in time that photons are emitted from a natural thermal source can be described through a Poisson distribution of arrival times [23]. This distribution is dependent primarily on the temperature of the source, the bandwidth of the observed light, and the read out rate of the detector. Once the parameters for photon distribution model have been established it is necessary to simulate the photons traversing through the simulated optical system.

3.6 Numerical Solutions of the Computational Model

Verification of the computation model is made though practical convergence studies and analytical solutions. These preliminary studies and analysis were necessary to confirm that the simulation algorithm was tailored to represent the optics, physics, and structure accurately. The parabolic reflector dish model had both an analytical and FEA solution for its maximum displacement at the vertex with the given loading and boundary conditions.

The mathematics involved with describing a static solution for deflections of a parabolic dish involves incorporating some higher order shape descriptions. Using simpler derivations of a spherical shell surface deformations gives a starting point to describe non-spherical objects. Adding a more refined geometric shape derivation adds the complexity necessary to establish an accurate solution to the reflective parabolic dish's maximum vertex value. Varying the thickness of the parabolic dish model gives another metric of comparison for the overall analysis.

Defining the extent that the varying scenarios in the simulation affects the photon statistics requires the mathematical interpretation of the second order correlation measurement. The second order correlation value is the metric used in II technology. Beginning with finding a baseline value for the test matrix comparison employs the correlation (similarity) measurement of the incoming sources photon time signatures to that of the detectors photon time signatures in the unperturbed dish state. A correlation/similarity value = 1, would mean that both the incoming and detected photons time signatures are exactly the same. The simulation algorithm approaches unity for the

unperturbed case but due to computational round off errors and limited mesh density a correlation value = 1, was not attainable as will be described in detail in Chapter 5.

3.7 Representation of the Numerical Solution

Quantifying how the structural perturbations of the parabolic reflecting dish affect the photon statistics captured at the focal plane requires graphic and tabular comparisons. Values of both the analytical and FEA displacement values are compared and contrasted. Spot diagrams of the photon distribution at the focal plane represent how efficiently light rays traverse both the unperturbed and distorted parabolic surface descriptions. Additional images of the deformed FEA reflector surfaces provide information giving insight into how photon path lengths are effected for the full simulation. Correlation values are derived from the combination of both, the source photons streams and that detector photon streams. Correlation value plots are the primary metric to evaluate the extent to which a deformed surface shape can affect an II correlation measurement.

Chapter 4

4) Analytical Model of Shell Deformation to Validate FE Analysis

Generally, reflecting surfaces are made extremely rigid or have supporting component that minimize deformations leading to optical aberrations. There are many aspects that must be considered in optimizing optical-mechanical design. The basic requirement for efficient reflectors are based in the following categories: cost of fabrication, materials, strength, stability, thermal properties, temporal response, and mass.

In the present study only the material thickness and orientation of the gravitational load was varied. There were two objectives to this analytical study:

1) To explore and understand differences between numerical (Finite Element Analysis) and closed-form analytical solutions, both of which involve assumptions and approximations.

2) To develop closed-form solutions; this could later be used in conjunction with other analytical equations provided in this dissertation on photon statistics and intensity correlation. These analytical expressions allow parametric evaluation of the variables.

4.1 Deformation of a General Thin Shell Due to Uniform Normal Pressure

This section presents the analytical expression for the deformation of a large spherical (or parabolic) shell with small thickness to size ratio where the bending stiffness is negligible and the ability to resist deformation (caused by internal pressure for example) is due to extension and curvature of the surface. Lemaitre G. N. [2009], discusses various

aberrations in optical telescopes and how they can be attributed to the deformation mechanics of the optics and supporting structure. The closed-form analytical framework provided by Timoshenko and Woinowsky-Kreiger [1987] lets one to validate FEM analyses and conduct parametric analyses that allows a system level assessment to be conducted. Examples of technical questions that can be assessed are:

1) What is the expected deviation from a parabola if a flat membrane shell is pressurized to create a parabolic surface used to focus an incoming beam to a detector array?
2) What is the surface anomaly caused by body forces such as gravity?

Figure 4.1 shows the element of a shell, at an angular position ϕ from the axis of revolution. N_ϕ is defined as the tangential force per unit length in the meridian plane (longitudinal direction). The pressure in the inward normal direction is defined as z. The force per unit length in a direction mutually perpendicular to N_ϕ and z is N_θ. Hence, the corresponding stresses in the shell are equal to N_θ/h and N_ϕ/h, where h is the shell thickness. The three forces N_ϕ, N_θ, and z are related by the equilibrium equation:

$$\frac{N_\phi}{r_1} + \frac{N_\theta}{r_2} = -z \qquad \text{[Eq. 4.1]}$$

A second equilibrium equation in the direction tangential to the meridian leads to:

$$\frac{d}{d\phi}\left(N_\phi r_0\right) - N_\theta r_1 \cos\phi = 0 \quad \text{[Eq. 4.2]}$$

Here r_1 is the radius of curvature of the meridian and r_2 is the normal distance from the point of interest to the axis of revolution. r_0 is the radius in the horizontal (latitudinal) plane and can be defined as $r_0 = r_2\, sin\phi$
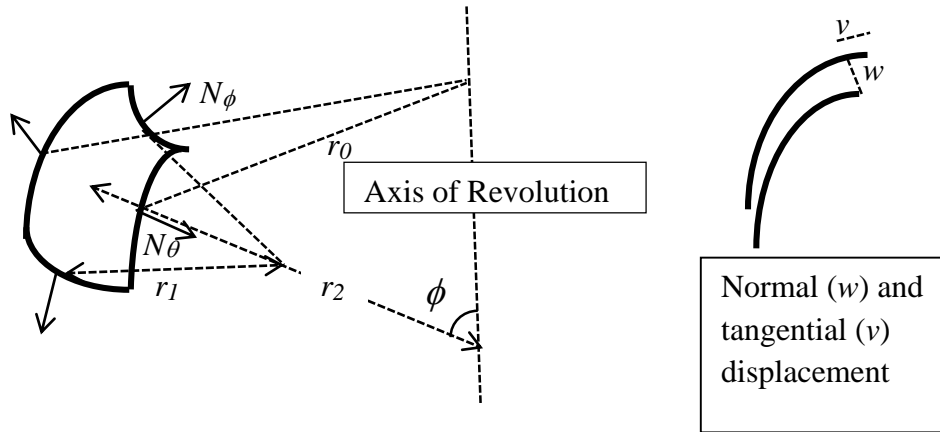
Figure 4.1 - Schematic of forces on a shell element

4.2 Specific Case of a Spherical Shell Supported at a Rim Under Gravity Load

Figure 4.2 shows a spherical shell supported at the rim ($\phi = \alpha$); for a shallow shell (relatively small α) the spherical and parabolic surfaces behave similarly.
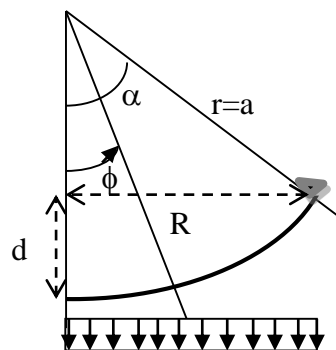
Figure 4.2 - Inverted schematic of a spherical telescope under gravity load

For a simple spherical shell $r_1 = r_2 = a$, and the solution due to a normal pressure q is given by Equation 11. This allows the variation of stresses in the membrane to be determined.

$$N_\phi = -\frac{aq}{1+cos\phi} \; , \quad N_\theta = aq\left(\frac{1}{1+cos\phi} - cos\phi\right) \qquad \text{[Eq. 4.3]}$$

For a parabolic shell $r_1 \neq r_2$, and Equations 4.1 and 4.2 must be used to obtain accurate solutions.

In order to determine displacement of the shell surface, the deformations v (tangential to the meridian) and w (normal to the surface) have to be evaluated from their relationships to the strains ε_ϕ and ε_θ along meridian and circumferential direction, respectively, via the elastic material properties E (modulus of elasticity) and μ (Poisson's ratio) [Eq. 4.4 & 4.5]:

$$\frac{dv}{d\phi} - vcot\phi = r_1\varepsilon_\phi - r_2\varepsilon_\theta \quad \text{[Eq. 4.4]}$$

$$\varepsilon_\phi = \frac{1}{Eh}\left(N_\phi - \mu N_\theta\right) \; and \; \varepsilon_\theta = \frac{1}{Eh}\left(N_\theta - \mu N_\phi\right) \quad \text{[Eq. 4.5]}$$

This leads to the relationship:

$$\frac{dv}{d\phi} - vcot\phi = \frac{1}{Eh}\left[N_\phi(r_1 + \mu r_2) - N_\theta(r_2 + \mu r_1)\right] = f(\phi) \; \text{[Eq. 4.6]}$$

The general solution of this is of the form:

$$v = sin\phi \left[\int \frac{f(\phi)}{sin\,\phi} d\phi + C\right]$$

The solution of which is given as:

$$v = K\left[sin\phi \ln(1 + cos\phi) - \frac{sin\varphi}{a + cos\varphi}\right] + Csin\phi, \quad where \; K = \frac{a^2 q \, (1 + \mu)}{Eh}$$

$$C = K\left[\frac{1}{1+cos\alpha} - \ln(1 + cos\alpha)\right] \qquad \text{(Eq. 4.7)}$$

The constant of the integration C was evaluated from the boundary condition $v = 0$ at $\phi = \alpha$.

Once v is determined, w can be determined from the relation:

$$w = vcot\phi - \frac{r_2}{Eh}(N_\theta - \mu N_\phi) \qquad \text{[Eq. 4.8]}$$

If one wanted to incorporate thermal expansion/contraction in the above analyses, it can be accomplished via Eq. 4.5, where the thermal expansion is added to the strain terms ε_ϕ and ε_θ. For example, in the specific case depicted in Figure 4.2 the exact solution to the deflections are as follows:

$$w = vcot\phi - \frac{a^2q}{Eh}\left(\frac{1+\mu}{1+cos\phi} - cos\phi\right) \text{ (Eq. 4.9)}$$

Where a is the radius and q is the applied out-of-plane load.

This general solution (Eq. 4.9) cannot be used for the specific application of this dissertation to find the displacement at the apex ($\phi = 0$), since from Eq. 4.8, $v = 0$, while $cot\phi = \infty$. So, it was necessary to revert to the original equations to derive the necessary solution valid for $\phi = 0$.

The relationship between the normal and tangential displacement is as follows:

$$w = \frac{\partial v}{\partial \phi} - r\varepsilon_\phi \qquad \text{[Eq. 4.10]}$$

Where ε_ϕ is the strain along the meridian.

Since v is known from Eq. 4.8, the derivative at the apex where $\phi = 0$ (note $sin\phi = 0$) is:

$$\frac{\delta v}{\delta \phi} = Kcos\phi\left[ln(1 + cos\phi) - \frac{1}{1+cos\phi}\right] + C\ cos\phi \quad \text{[Eq. 4.11]}$$

The steps in determining the deflection at the vertex based on these derivations are:

1) Determine C from the boundary condition (value of α) using Eq. 4.7

2) Determine ε_ϕ and $\delta v/\delta\phi$ using Eq. 4.3, 4.5, and 4.11

3) Use Eq. 4.10 to determine w.

4.3 Numerical Input

The specific parameters for the modeled reflector were determined as follows:

Selected: Radius of the rim (R) = 0.78m, depth, d (vertex to the plane of the rim) = 0.234m

Assumed: A small segment of a parabolic curve approaches a circular solution at the vertex

Determined: The best fit spherical surface to this reflector has a Radius (a) = 1.417m

Therefore, the boundary is at α = 33.4°.

Using the following values:

Thickness (h) = 0.1mm = 10^{-4} m, E = 6MPa, μ = 0.47, and density = 1290Kg/m^3

From Eq. 4.7 calculating $C = K\left[\frac{1}{1+cos33.4°} - \ln(1 + cos33.4°)\right] = -0.062K$

From Eq.4.6, $\frac{\delta v}{\delta\phi} = Kcos0° \left[Ln(1 + cos0°) - \frac{1}{1+cos0°}\right] + C\ cos\varphi = 0.193K - 0.062K = 0.131K$

From Eq.11, $N_\phi = N_\theta = -aq/2$. From Eq.4.5 $\varepsilon_\phi = -aq(1-\mu)/2Eh$

Gravity load, q (= density x gravity x thickness) = 1,290 x 9.81 x 10^{-4} = 1.265N/m^2

From Eq.4.9,

$w = 0.131K + a^2q(1-\mu)/2Eh = \frac{1.417^2\ x\ 1.265}{6\times10^6\times10^{-4}}\left[(1.47\ x\ 0.131) + (1 - 0.47)/2\right] =$ **0.0019m**

(1.9mm). This is the analytic solution to the maximum displacement at the vertex of the surface with the given boundary conditions and loads.

4.4 Analytical Evaluation Pertaining to a Paraboloid

Figure 4.3 shows a parabolic shape with the chosen Rim radius (R) = 0.78m and Depth (d) = 0.234m. The parabola therefore has the equation $y^2 = 4ax$, where $a = 0.65$m is the focal distance (distance from the vertex to the focal plane).
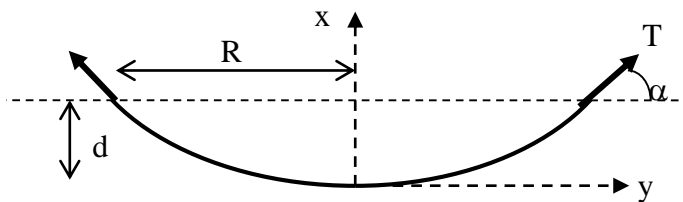
Figure 4.3 Schematic of a Parabolic Reflector

From analyzing the parabolic equation the following equation can be derived:

$$\frac{\partial x}{\partial y} = \frac{2y}{4a}, \ \ so \ \left(\frac{\partial x}{\partial y}\right)^2 = \frac{y^2}{4a^2} \quad \text{[Eq. 4.12]}$$

The length of the arc from the rim to the vertex is obtained by integration:

$$S = \int \partial s = \int \sqrt{\partial x^2 + \partial y^2} = \int \sqrt{1 + \left(\frac{\partial x}{\partial y}\right)^2}\, \partial y = \int_0^{0.78} \sqrt{1 + \frac{y^2}{4a^2}}\, \partial y \quad \text{[Eq. 4.13]}$$

Using the binomial expansion $\sqrt{1 + z} = 1 + \frac{z}{2} - \frac{z^2}{8} + \cdots$ this integration can be approximated as:

$$S = \int_0^{0.78} \left[1 + \frac{y^2}{8a^2} - \frac{y^4}{8 \times 16a^4} + \cdots\right] \partial y = \left[y + \frac{y^3}{24a^2} - \frac{y^5}{640a^2} + \cdots\right]_0^{0.78} \quad \text{[Eq. 4.14]}$$

It can be seen from Eq. 4.14 that when a load is applied and the vertex of the parabola shifts outwards, the second and third terms are what contribute to the change in

the arc length (S). For the initial parabolic shape S = 0.8268m and 0.8243m with 2nd and 3rd terms of Eq. 4.14. When this parabolic shell is deformed under gravity load, the rim circumference (y= 0.78m) does not change, but the vertex moves causing a change in the focal length 'a'.   It can be shown that for small changes in the vertex (a few mm) the change in the second term is negligible compared to the change in the third term, i.e. only the third term is sufficient in evaluating the change in the arc length (related to strain) as the shell deforms. As shown in Figure 4.3, the gravity load is countered by the X-component of the forces along the rim.

The gravity force = Surface area x q $\cong$ 2πRdq = 2πx0.65 x 0.234 x 1.265 = 1.21 N.

At the rim $\delta x/\delta y = y/2a$ = 0.78/(2 x 0.65) = 0.6 = tan α; so α = 31°

Furthermore, if T is the tension force along the meridian, (Figure 4.3), from equilibrium T sin31° = 1.21N.

The rim circumference is 2π X 0.78 = 4.9m, and the material thickness is 10^{-4}m,

Therefore σ_ϕ = 1.21/(sin 31° x 4.9 x 10^{-4}) = 4,795 N/m^2 and $\varepsilon_\phi = \sigma_\phi/E$ = 8.0 x 10^{-4}.

For example, suppose the vertex moves under load such that the new depth is d', and the focal length is a'.

Using Eq.4.14, Meridian strain $\varepsilon_\varphi = \dfrac{\partial S}{S} = \dfrac{y}{24S}^3 \left(\dfrac{1}{a^2} - \dfrac{1}{a'^2}\right) = \dfrac{0.78}{24\times0.8268}^3 \left(\dfrac{1}{0.65^2} - \dfrac{1}{a'^2}\right) =$ 8 × 10^{-4}

Solving Eq, 4.14 with 'a' = 0.6455m. Note that as the vertex moves out and the focal point moves in.

Once the new 'a' is determined, the value of x (for y = 0.78m) can be determined from the equation for a parabola (y^2 = 4ax); x = $y^2/4a$ = 0.78^2/(4x0.6455) = 0.2356m.

So, the vertex moved by 0.234-0.2356 = **0.0016m = 1.6mm**

4.5 Comparison of Various Analyses

The analysis based on the circular membrane shell approximation resulted in the largest deformation (1.9mm). Membrane theory assumed that the boundary is free to move in the circumferential direction, which results in greater overall displacement. The circular shape is also an approximation of the paraboloid. The FEM analysis had fixed boundaries and the 'thin shell' elements used were not 'membrane' elements; i.e. they had some bending stiffness. These two issues contribute to a smaller overall analytically derived maximum deflection (1.6mm).
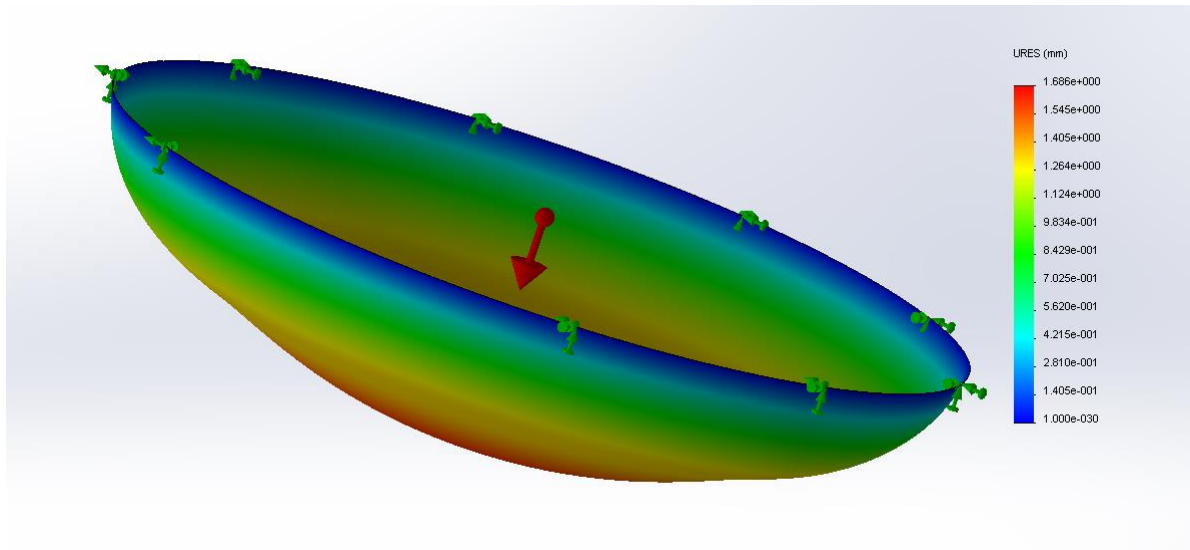
Figure 4.4 - Exaggerated Displacement of Horizontal Gravitational Load

The parabolic shell analysis better captures the actual shape and the resulting maximum displacement (1.6mm) when compared to that of the FEM analysis (1.686mm -

Fig 4.4). However, the analytical does not capture the effect of the changing radius of curvature of a parabola from the vertex to the supporting rim. The extent of error this may introduce could be sufficient to explain the difference between the analytical derived solution compared to the FEM maximum displacement [37, 38].
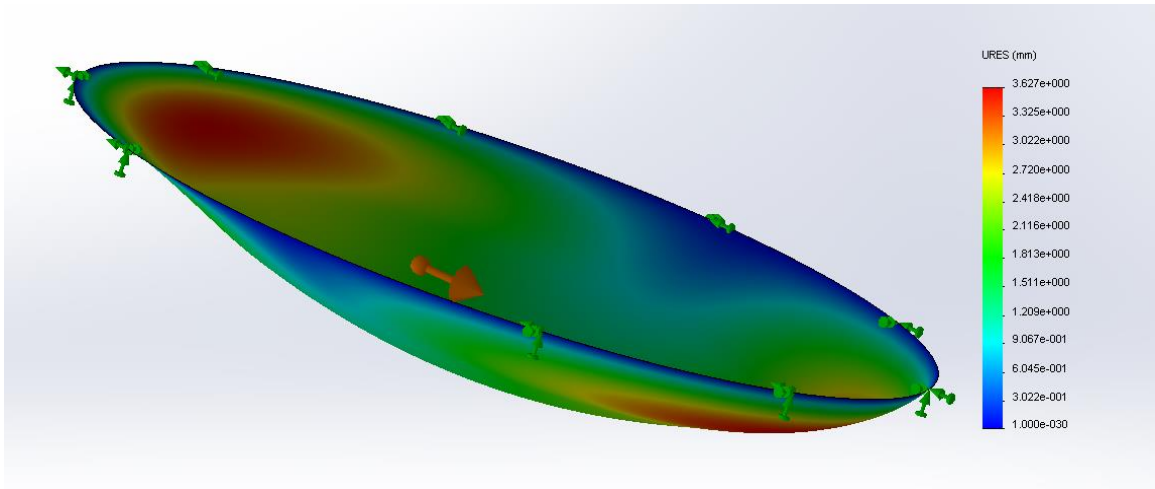
Figure 4.5 - Exaggerated Displacement of Vertical Gravitational Load

Chapter 5

5) Simulation Algorithm and Software Interfacing

---

1) Physical System

- **Focal Reflecting Parabolic Disk an Intensity Interferometry Receiver**
- **Coupling mirror distortions to detected photon statistics**
- **Test Matrix**

---

2) Conceptual Modelling of the Physical System

- **Distant Photon Emitting Point Source**
- **Light represented as parallel rays to the focal axis**
- **Reflecting off an unperturbed/distorted parabolic surface**
- **Impinging on a focal plane detector.**

---

3) Mathematical Modeling of the Conceptual Model

- **Photon represented as particles with a natural distribution**
- **Parabolic reflector geometry**
- **Finite element analysis for reflector loading, boundary conditions, and materials**

---

4) Discretization and Algorithm Selection for the Mathematical Model

- **Poisson distribution of arrival times and flux based on physics**
- **Geometric optics**
- **Drafting the Parabolic Reflector**
- **Analytic solution for surface of revolution distortions due to loading scenarios**
- **Meshing the Reflector and performing FEA**
- **Extracting Surface Nodes to import into triangulation algorithm to represent surface for geometric optical analysis**

```
┌────────────────────────────────────────────────────────────┐
│         6) Numerical Solution of the Computer Model          │
│                                                              │
│     •   FEA comparison                                       │
│     •   Second order correlation measurement                 │
│                                                              │
└────────────────────────────────────────────────────────────┘
```

```
┌────────────────────────────────────────────────────────────┐
│         7) Representation of the Numerical Solution          │
│                                                              │
│     •   Error                                                │
│     •   Graphs                                               │
│     •   Conclusions                                          │
│                                                              │
└────────────────────────────────────────────────────────────┘
```

5.1 Assumptions for Simulating an Intensity Interferometer

Many avenues of research could have been performed to answer various scientific questions but this dissertation focused on answering the general thesis statement, how would the correlation of an intensity field change as a large light weight reflective structure deforms? Many assumptions were made and their justifications will be presented based on the requirements of the simulation and/or the analysis.

The simulated optical setup will consist of a focal reflector with similar dimensions to the original II instruments. The simplification of this analysis begins with assuming that

a geometric ray tracing analysis is established. This assumption treats light as particles, not waves, meaning diffraction effects do not contribute to the physics of the simulation. Another assumption is that all the light is propagating directly parallel to that of the optical axis of parabolic reflecting surface.

Additionally, the reflector has been selected to be a thin parabolic dish. The surface of the dish although discretized into triangular elements, is perfectly reflecting. The detector will absorb all photons impinging on its surface and will be represented as an infinite XY plain located at $z = .65$ and the parabolic surface vertex at $z = 0$.

5.2 Basic Dynamic Model Description

This research is based on the physics of intensity interferometry and photon statistics emanating from a stellar point source to a parabolic focal detector system. Understanding the changing photon statistics gives valuable information that can be used to improve the design and efficiency of intensity interferometers. The source of incoming photons are emitted randomly throughout a light emitting disk with a radius equal to that of the parabolic reflector with a radius of 0.78m and a focal point of 0.65m, similar to the original optical intensity interferometer [2]. The light emission can be conceptualized as a column of light particles coming from a distant source (Figure 5.1). The emission disk will be placed above the X-Y plane at a distance of 2m from the origin. The photons travel to the reflector along the vertical Z-axis and have a random nature to their spatial extent and temporal characteristics. Investigating how the detector output and the surface spatial perturbations effect on the time of flight of the photons is the purpose of the simulation.

47
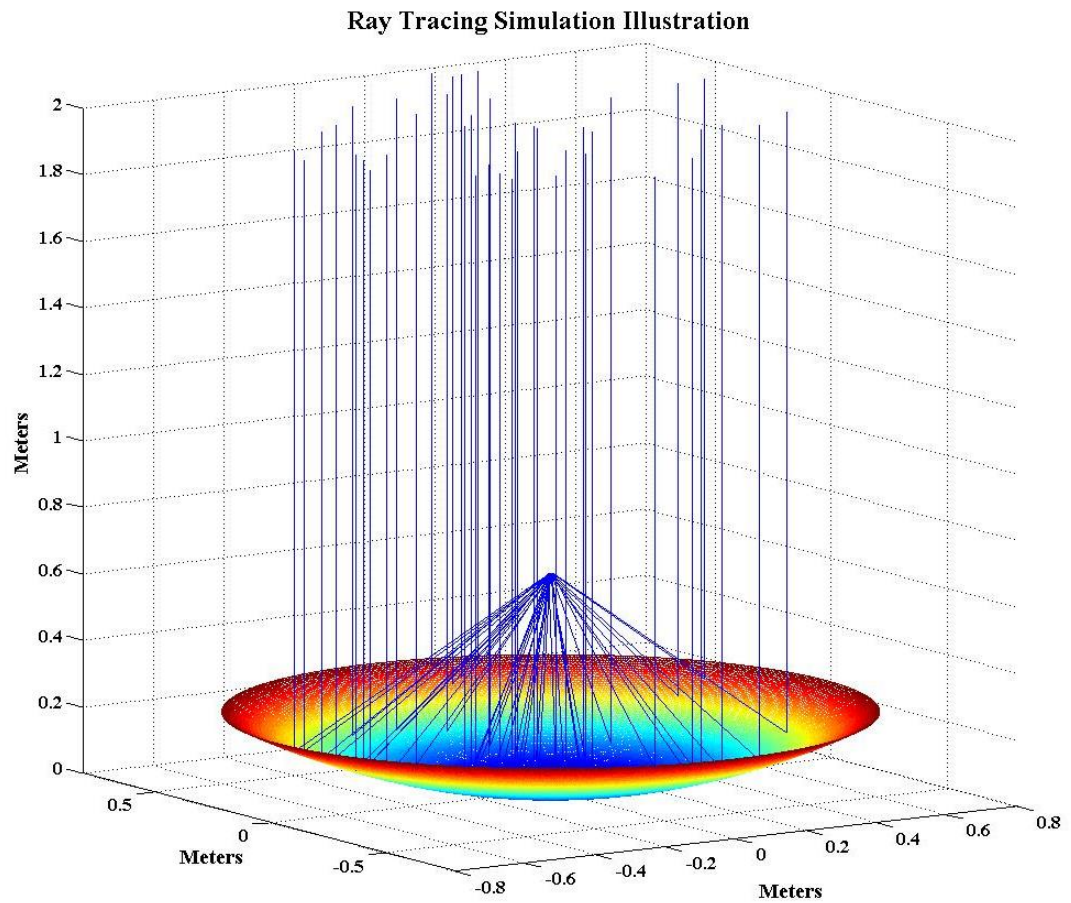
Figure 5.1 - Ray Tracing Model

The light being collected has a natural Poissonian distribution for the frequency (not related to the color) that the photons are emitted from a simulated thermal source (star light). The incoming photons are reflected off a parabolic dish with the unique characteristic of focusing all incoming parallel light to a single point. Due to the nature of intensity interferometry an image is not preserved to the focal plane, allowing fewer constraints on the precision of the smoothness of the reflecting surface. An analysis of varying the focal length of a simulated detector and surface the shape of the parabola will give insight into their effect on the statistics of the detected photon streams.

48

5.3 Focusing Properties of a Two Dimensional Parabola

A basic description is necessary to describe the unique focusing characteristics of a parabolic reflector. A two dimensional curve is drawn starting at the origin and extending out along a line defined by a parabolic curve. Beginning in the x-y plane, a curve represents a reflective surface. Symmetrical reference can be noted by a y axis reflection; i.e. y(−x) = y(x). An additional rotation can be made about the y-axis to form a 3-dimensional parabolic dish which is defined as a surface of revolution. Projecting that surface back to the x-y plane gives a curve that will be used in ray propagation and the subsequent reflection scenario.

Consider parallel light rays that strike a curved mirror surface (Figure 5.2). The first ray is initially propagating in a direction parallel to the y-axis. It then strikes the mirror and forms an angle of incidence with respect to the normal, which is perpendicular to the tangent at point P(x,y). A perfectly reflecting surface uses the law of reflection where the angle of incidence equals the angle of reflection, implying the ray reflects and is incident at the focal point F(0,f). An additional ray example traverses straight down the y-axis reflecting at point O(0,0) and is incident at point F(0,f) [37].
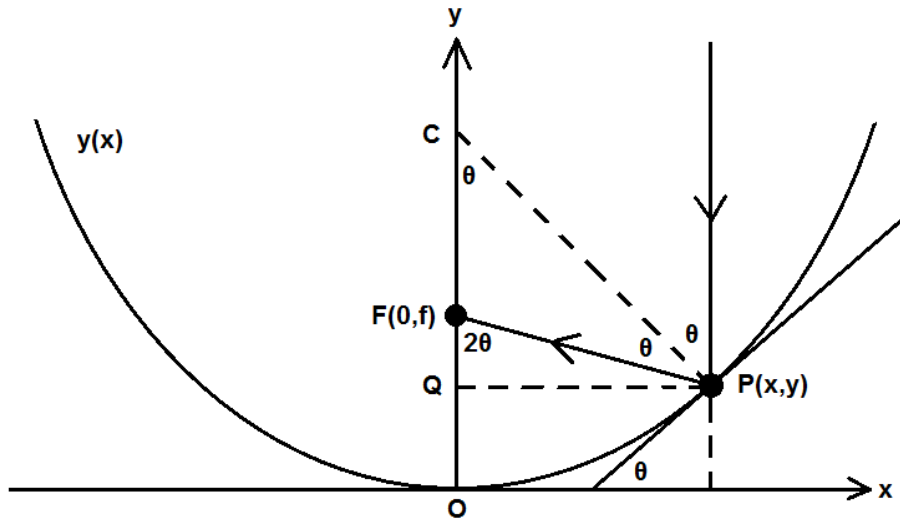
Figure 5.2 - Focusing Properties of a Parabola

A tangent line is defined at P and forms an angle with the x axis. Which is defined by:

$$\tan\theta = \frac{dy}{dx} \qquad \text{[Eq. 5.1]}$$

The derivative of the curve y(x) at point P. With the angle ∠FCP equal to θ, the original light rays are parallel and it can be concluded that ∠QFP is equal to 2θ. This means that the line FQ is given by x/tan2θ and the focal length f is defined as:

$$f = y + \frac{x}{\tan 2\theta} \qquad \text{[Eq. 5.2]}$$

Employing the identity:

$$\tan 2\theta = \frac{2\tan\theta}{1-\tan^2\theta} \qquad \text{[Eq. 5.3]}$$

Combining equations 5.2 and 5.3 yields:

$$f = y + \frac{x(1-\tan^2\theta)}{2\tan\theta} \qquad \text{[Eq. 5.4]}$$

And for a parabola:

$$y = Ax^2 \qquad \text{[Eq. 5.5]}$$

In which $dy/dx = 2Ax$. Plugging these definitions into equation Eq. 5.4 gives

$$f = Ax^2 + \frac{x(1-4A^2\,x^2)}{4Ax} = \frac{1}{4A} \qquad \text{[Eq. 5.6]}$$

5.4 Ray Tracing Algorithm

A 3-dimensional geometric ray tracing algorithm has been developed using vector notation for a single focal system. Figure 5.3 depicts a psuedo 3-dimensional surface, where vector terms are used to represent photon paths and the triangular element is the reflective surface with its associated normal unit vector.
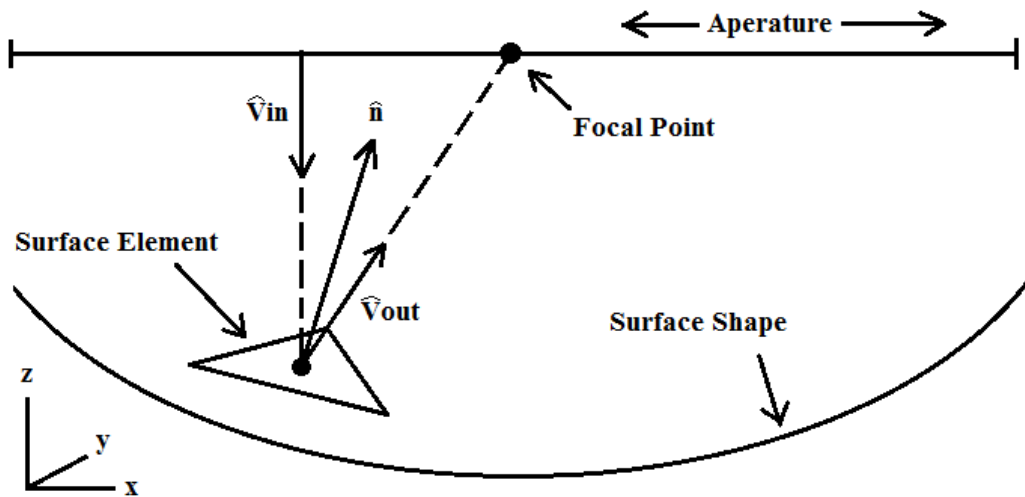
Figure 5.3 - 3-Dimensional Surface Vector Reflection

The simulation incorporates a photon stream (column of photons) that reflects off a perfect parabolic reflector and is absorbed on a detector.

$$\boldsymbol{x} = \begin{pmatrix} x \\ y \\ z \end{pmatrix} \qquad \text{[Eq. 5.7]}$$

51

$\boldsymbol{x}$ is a column vector, and a vector with a '^' (as in $\hat{\boldsymbol{x}}$) is a unit vector. When necessary a transpose will be incorporated to satisfy Matlab software syntax. Starting with a parabolic surface defined by the equation:

$$z = f(x, y) = A\, r^b = \frac{1}{2*F}\left((x^2 + y^2)^{1/2}\right)^b \qquad \text{[Eq. 5.8]}$$

The vertex of the parabola will have coordinates (0,0,0) and F is the focal length. The incoming light is traveling in some direction, $\hat{\boldsymbol{v}}_{in} = (0,0,-1)^{\text{T}}$. Because the mirror has a certain radius it is necessary to check the condition that the photons actually reflect off the parabolic dish using the following inequality:

$$P_x^2 + P_y^2 \leq R_m^2 \qquad \text{[Eq. 5.9]}$$

Where P_x and P_y are a specific point on the reflector and R_m is the overall radius of the detector.

The output direction of the light, $\hat{\boldsymbol{v}}_{out}$, is given by the equation:

$$\hat{\boldsymbol{v}}_{out} = \hat{\boldsymbol{v}}_{in} - 2(\hat{\boldsymbol{n}}^t \cdot \hat{\boldsymbol{v}}_{in})\hat{\boldsymbol{n}} \qquad \text{[Eq. 5.10]}$$

Where $\hat{\boldsymbol{n}}$ is the unit normal vector of the curve at the point **p**. The formula for $\hat{\boldsymbol{n}}$ is given by first computing the direction of the unit normal at the point **p**:

$$\boldsymbol{n} = \begin{pmatrix} (\partial_x f)(p_x, p_y) \\ (\partial_y f)(p_x, p_y) \\ -1 \end{pmatrix} \qquad \text{[Eq. 5.11]}$$

Then normalizing:

$$\hat{\boldsymbol{n}} = \frac{\boldsymbol{n}}{\|\boldsymbol{n}\|} \qquad \text{[Eq. 5.12]}$$

Where the norm of a vector is given by $\|\boldsymbol{n}\| = \sqrt{\boldsymbol{v}^t \cdot \boldsymbol{v}}.$

This makes every point on the travel line from the parabolic reflection to that of the detector equal to:

$$a\,\widehat{\boldsymbol{v}}_{out} + \boldsymbol{p} \qquad\qquad\qquad \text{[Eq. 5.13]}$$

In which a is real scale factor and **p** is the point of reflection.

Now it is necessary to model where the detector lies. This is specified by a normal vector **d,** which gives the direction that the detector is pointing and a location vector **r.** Note that **d** does not have to be a unit vector. The plane of the detector (Figure 5.6) is the set of solutions to the equation:

$$\widehat{\boldsymbol{d}}^t \cdot (\mathbf{x} - \mathbf{r}) = 0 \qquad\qquad \text{[Eq. 5.14]}$$

Solving for **x** while following the condition that any solution of the vector **x** must satisfy the following inequality:

$$\|x - r\| \le R_d \qquad\qquad \text{[Eq. 5.15]}$$

Where R_d is the size of the detector.

To find where our reflection line intersects the detector, place Eq. 5.13 for a point on the detector (the **x** vector in Eq. 5.14):

$$\widehat{\boldsymbol{d}}^t \cdot \big((\,a\,\widehat{\boldsymbol{v}}_{out} + \boldsymbol{p}) - \boldsymbol{r} \big) = 0 \qquad \text{[Eq. 5.16]}$$

By distributing the dot product **a** can be solved for. It is important to remember if the detector is parallel to the reflected light, then there is no intersection. Solving for the scalar **a** gives:

$$\boldsymbol{a} = \frac{\widehat{\boldsymbol{d}}^t \cdot (\mathbf{r} - \mathbf{p})}{\widehat{\boldsymbol{d}}^t \cdot \widehat{\boldsymbol{v}}_{out}} \qquad\qquad \text{[Eq. 5.17]}$$

Noting that $|a|$ has the interpretation of being the distance from where the light strikes the mirror to where it intersects the detector. Now it is possible to get the time of

flight for the light from simulated emission plane to being reflected off the reflector and eventually hitting the focal plane at point:

$$s = \frac{\hat{d}^t \cdot (\mathbf{r} - \mathbf{p})}{\hat{d}^t \cdot \hat{v}_{out}} \, \hat{v}_{out} + \mathbf{p} \qquad \text{[Eq. 5.18]}$$

By substituting all the vectors into Equation 5.18, a closed form solution for the point of detection s at the focal plane is developed.
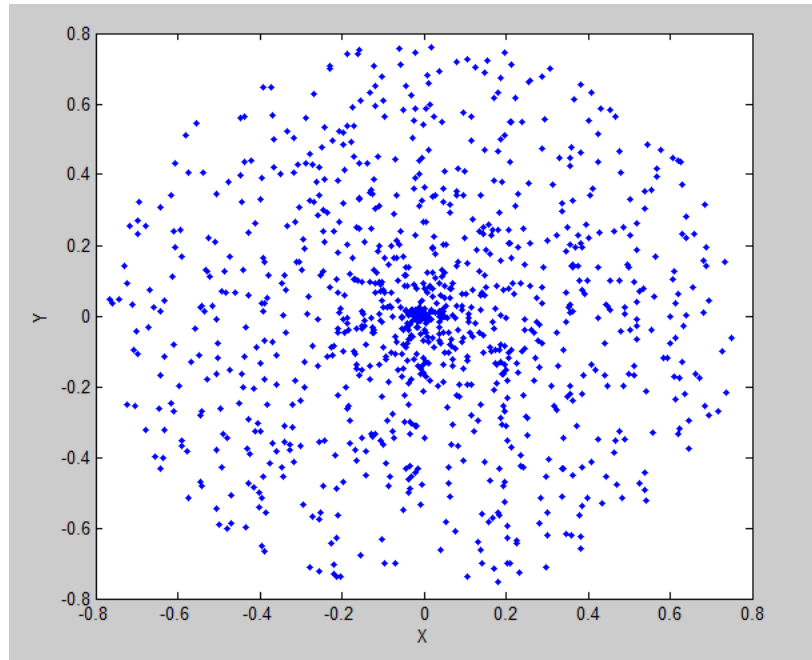
5.5 Random Photon Emission

An algorithm was developed using Matlab mathematical modeling software to obtain emission points on a disk. The random nature of emission points is how light is emitted on a stellar surface, traversing through space, and enters an aperture of a reflective mirror. Equation 5.19-5.23 are the calculations necessary for the random point generator. Theta is an angle that is randomly generated between 0 and 2*pi. In order to not have a concentration of points at the center (Figure 5.4) it is important to have a square root factor on the random radius variable (Figure 5.5). The *rand* Matlab function generates a number between 0 and 1, n is number of points, dradius is the radius of the incoming light field (0.78m), x and y are the positional points on the emitting dish.
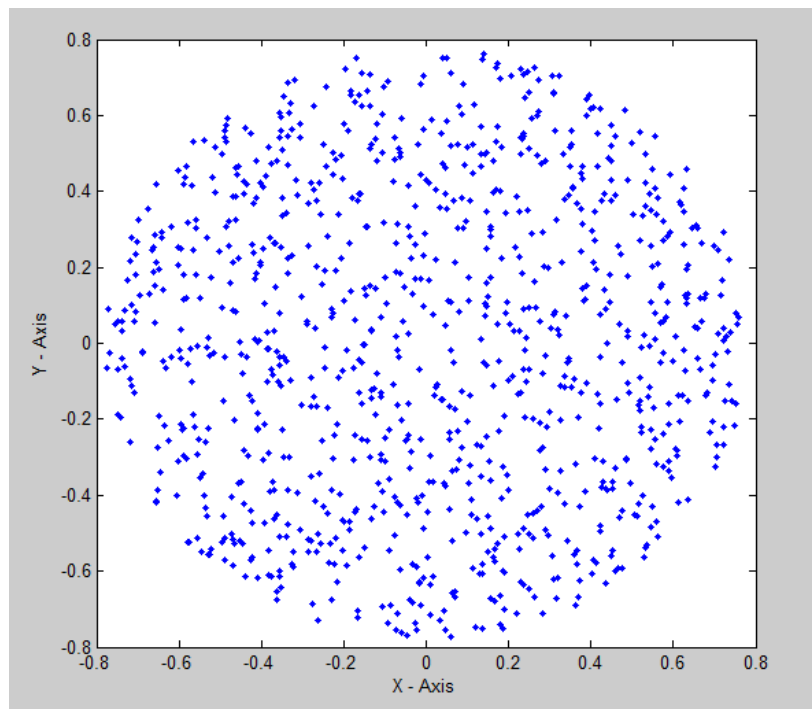
theta = rand(1,n)*(2*pi);   [5.19]
r = sqrt(rand(1,n))*dradius;   [5.20]
x = r.*cos(theta);   [5.21]
y = r.*sin(theta);   [5.22]

Figure 5.4 - Centralized Emission Points


Figure 5.5 - Random Emission Points

55

5.6 Random Number Distribution

To obtain a baseline on the temporal distribution of impinging photons on the focal parabolic system, a simplified version of the photon statistics was incorporated. A random number distribution of **N** time intervals was developed. The algorithm was established to use 1's as a photon emission and a 0's as a null emission with the time between a photon/null emissions defined as $5e^{-11}$ seconds. Using a mean of 0.5 implies that there will be the same amount of photon emission as null times, roughly **N/2** photons. This distribution has the greatest likelihood that five photons will be detected in ten time intervals, with a lesser chance of ten photons being detected in the same time interval. The following Matlab code can be modified and used with varying mean values to define an assumed Poisson distribution of 1's and 0's:

$$t1 = rand(n,1).*sign(rand(n,1) - .5) \qquad [5.22]$$
```
                    for i = 1:n
                    if t1(i) >=0;
                    k1(i) = 1;
                    else if t1(i) < 0;
                    k1(i) = 0;
```

Combining the random distributions involves addressing the physics of the emission process. The stream of photons coming from an extremely distant ($\sin \theta = \theta$) source are all coming in parallel to one another along the z-axis as that of Figures 5.1 and 5.6. The disk of random emission points is combined with the randomly distributed photon emission times. Thus, a photon emission has an assigned time tag and a point on the emission disk. An array of photon vectors ($\hat{\boldsymbol{v}}_{in} = (0,0,-1)^T$) is assigned to each photon emission time tag to eventually reflect off of the parabolic dish and be received at the

detector. A two-fold stochastic emission process is defined incorporating the random nature of emission positions and times.
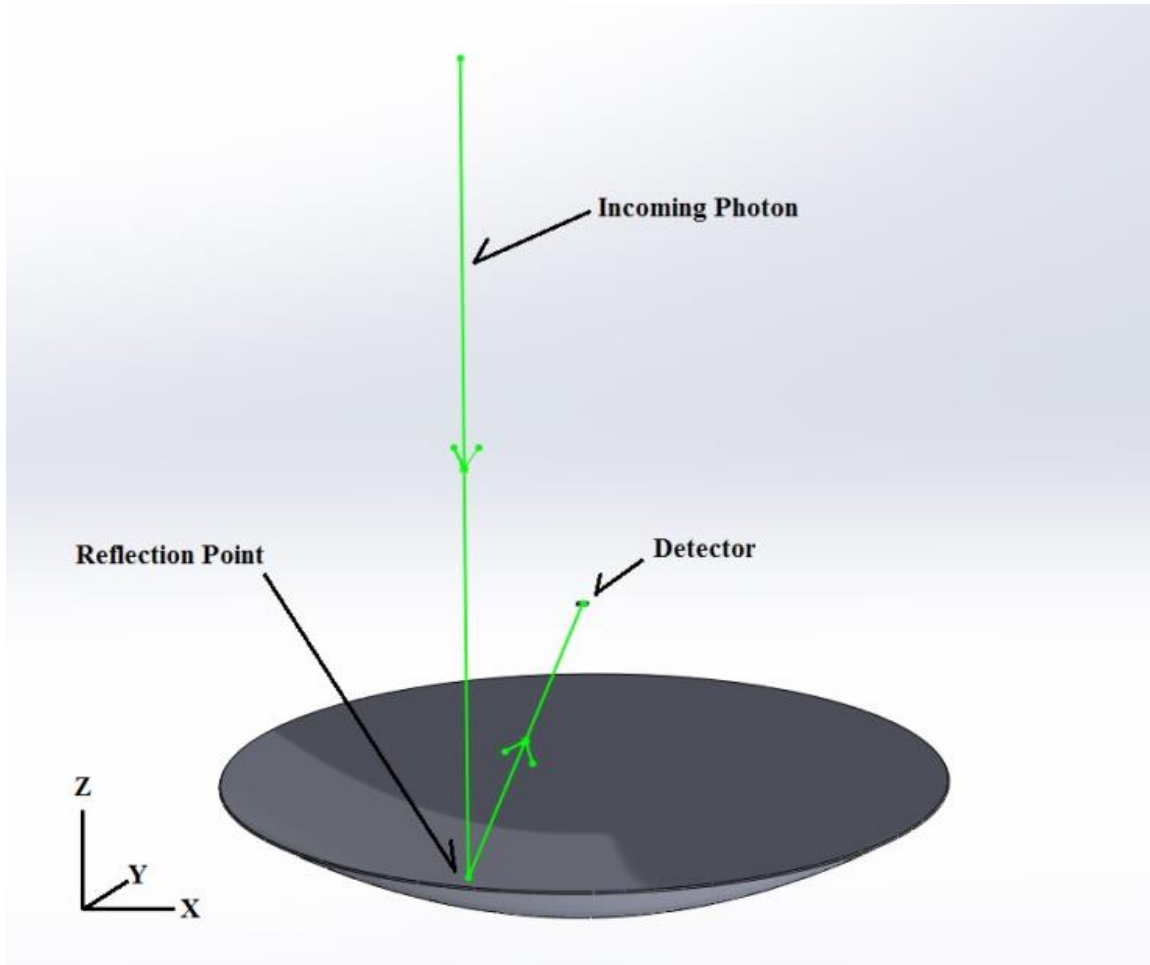
Figure 5.6 - Parabolic Surface
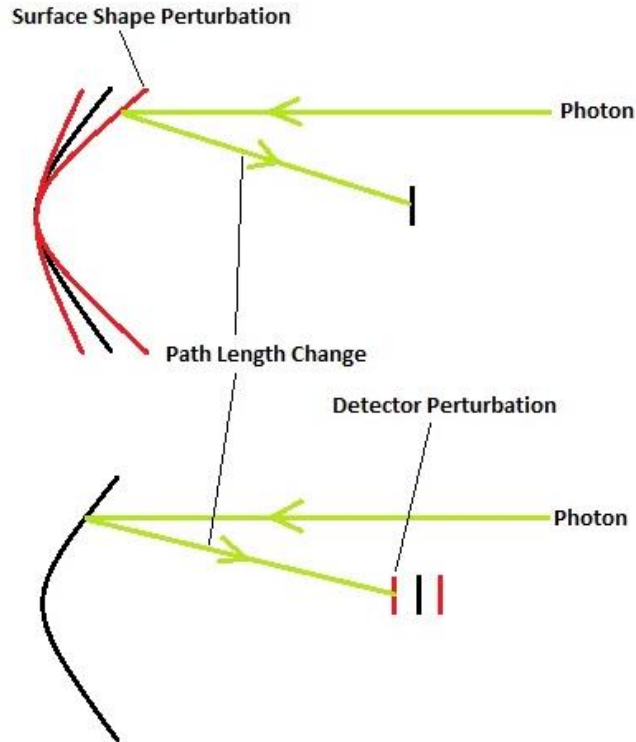
Figure 5.7 - Surface and Detector Perturbations

5.7 Parabolic Focus Confirmation

To confirm that the initial mathematical algorithm was correctly implemented, the point spread distribution on the focal plane was evaluated at various detector focal plane distances. Figure 5.8 shows the point distribution plots going clockwise from the top left 0.63m,0.64m,0.65(Focal Point),0.651m,0.6525m, and 0.655m for the various focal distances. The focal point confirms the nature of a perfect parabolic dish which reflects all z-axis parallel rays to one specific distance (point) as in the top right image of Figure 5.8.
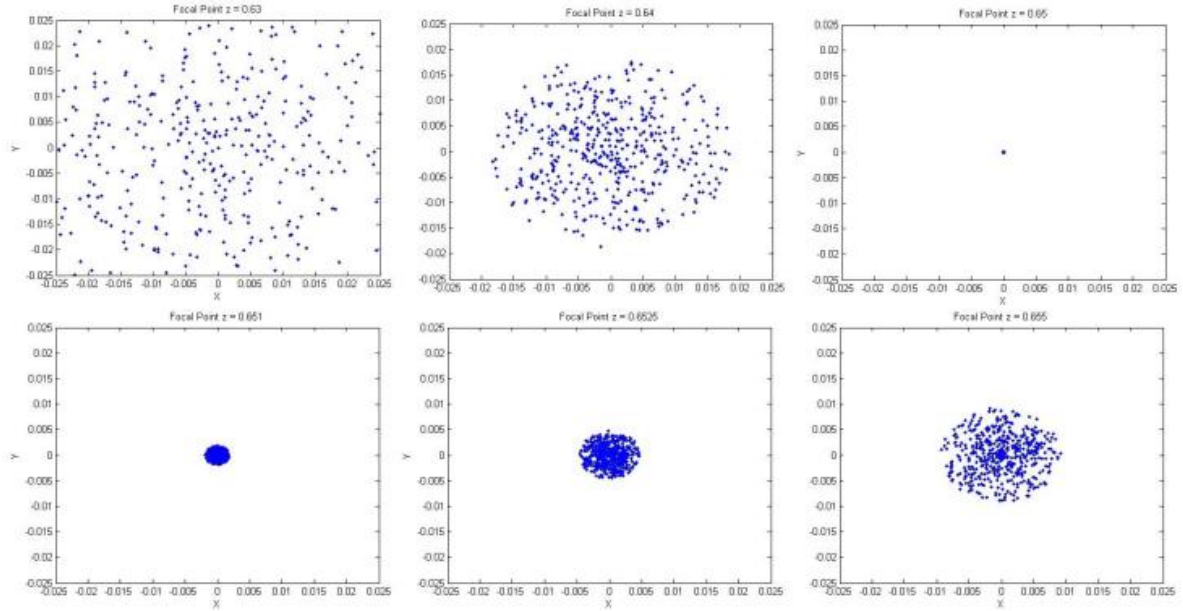
Figure 5.8 - Varying Focal Point Spread Distributions (each axis 5cm^2)

All light coming in parallel to the z-axis of the parabolic dish (top-right Fig 5.8) will fall eventually on the detector exactly at its focal length. All photons reflected off the perfect parabolic surface will be concentrated at a single point on the detector. This specific concentration at the focal point may be impractical for actual detectors due to material and electronic limits in the design of current detectors. The total distance travelled for all the photons is the length travelled to the parabolic reflector from the emitting disk (2m) then reflecting off the surface until hitting the detector (0.65m) for a total of 2.65 for each photon (Figure 5.9). Although the constant 2.65m travel distance for all photons traversing the focal system is a null result, it provided a direct confirmation that the simulation algorithm was valid.
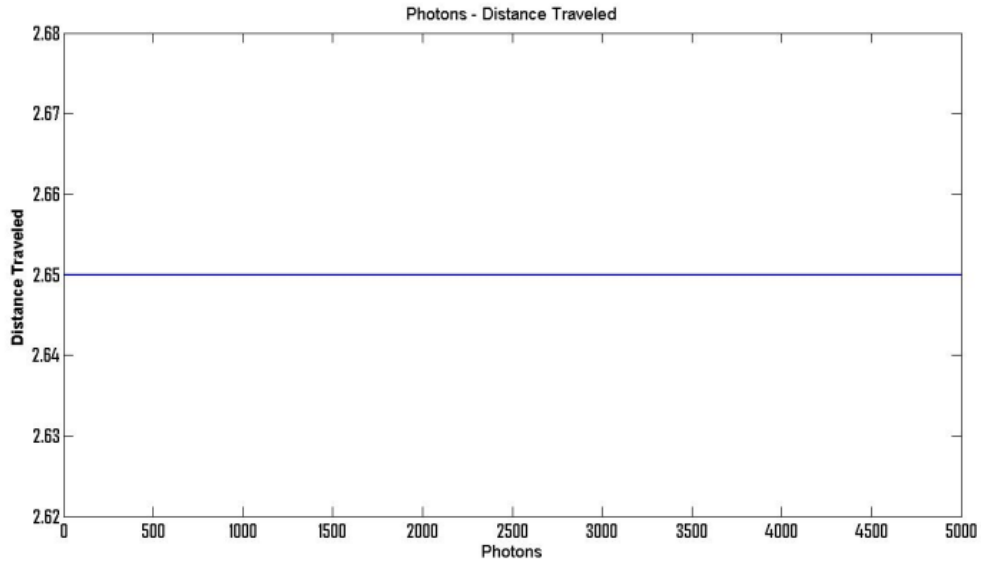
Figure 5.9 - Perfect Parabola/Photons Travel Distance

A perturbed surface was developed by varying the exponent in the parabolic surface of Equation 5.8. This original analysis incorporates a focal plane compared to an actual instrument that has a fixed detector size. The exponent of Equation 5.8 was adjusted incrementally to determine the parabolic surface shape at which the distance travelled by the photons falling on the focal plane would begin to significantly deviate from that of a perfect focal parabolic reflector. Figure 5.10 graphs the distance travelled by the photons through the focal system and lists them from the baseline of 2.65m to 0.006m greater than 2.65m for the *b* parameter exponent value of 2.1 in Eq. 5.8.
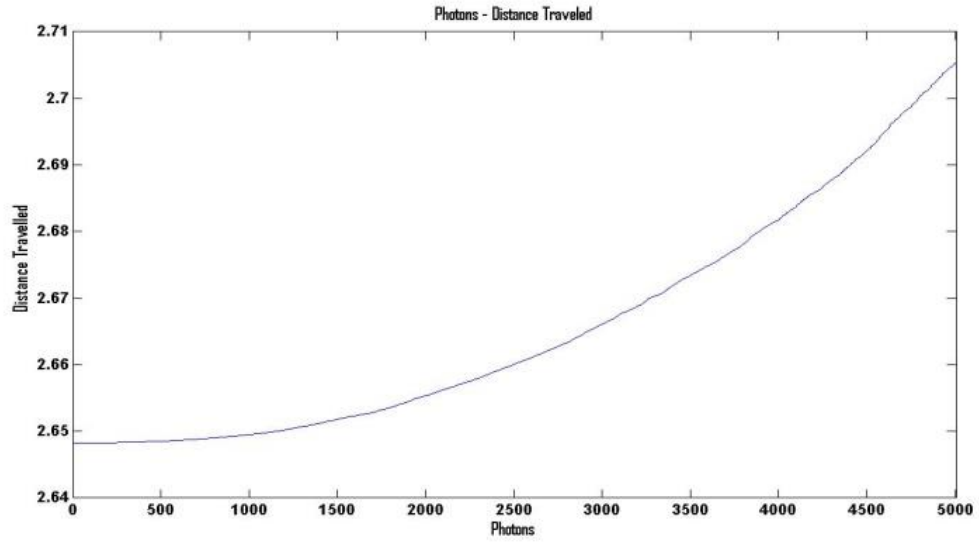
Figure 5.10 - Perturbed Parabola/Photons Travel Distance

Figure 5.11 shows the dispersion of photons hitting the plane of the detector located at .65m from the vertex of the parabolic surface. The surface was defined using Eq. 5.8 by varying the b parameter from top-left moving clockwise, b = 1.9, 1.99, 1.999, 2, 2.05, and 2.1. It has been shown that if the surface deviated from the perfect parabolic shape on the outer edges of 0.003m. This would inevitably change the travel time of the incoming photons on the focal plane, thereby changing the statistics of the detected photons.
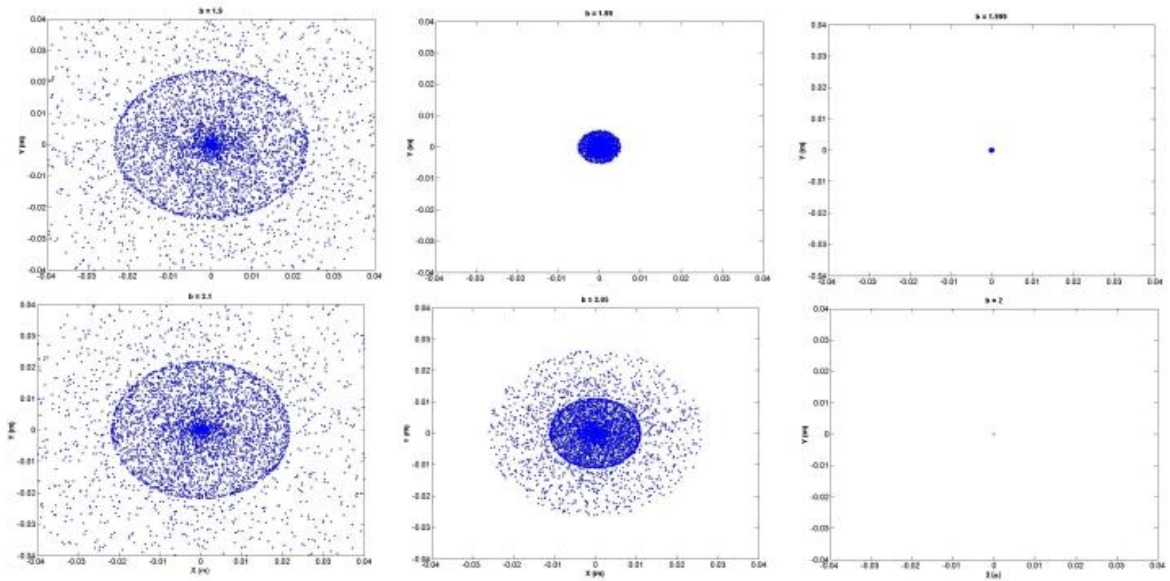
Figure 5.11 - Focal Plane for Various b parameters (axis 5cm^2)

5.8 Detected Photon Statistics

All the simulations used the same data set of emission points and time of emission. The statistics of the detected photons was evaluated using mean and standard deviation measurements with Matlab mathematical software. All perturbed scenarios were evaluated including incorporating the perfect parabola/focal point model. Eq. 5.22 was used as a distributed random number generator with a mean of 0.5. This was confirmed by taking the mean of **k1**, the random photon emission spacing's as in Eq. 5.22.

Table 5.1 is a list of the mean and standard deviation of photon travel times (PTT). The focal plane fixed at 0.65m and parabolic shape exponent of 2 (Eq. 5.8) creates the perfect parabolic shape used as the baseline for the analysis. The aforementioned perturbed scenarios describe that the statistics of the photon detection times do change with the various structural and detector perturbations. The mean PTT is the time it takes a photon

to travel 2.65m. Dividing by the speed of light (299,792,458 m/s) gives 8.8394e^-9

seconds. Also, the standard deviation for the baseline focal plane (.65m) and surface shape

(b = 2) has a value of 0, indicating that there is no change to the PTT and confirming that

all photons travel the same distance as in Figure 5.9.

Parabola Parameters	Mean (Photon Travel Time) PTT	Standard Deviation PTT
Focal Plane = 0.63	8.74E-09	2.12E-11
Focal Plane = 0.64	8.79E-09	1.06E-11
Focal Plane = 0.65	8.84E-09	0.00E+00
Focal Plane = 0.651	8.84E-09	1.06E-12
Focal Plane = 0.6525	8.85E-09	2.65E-12
Focal Plane = 0.655	8.86E-09	5.31E-12
b = 1.9	8.78E-09	5.65E-11
b = 1.99	8.83E-09	5.62E-12
b = 1.999	8.84E-09	5.62E-13
b = 2	8.84E-09	0.00E+00
b = 2.05	8.87E-09	2.80E-11
b= 2.1	8.89E-09	5.57E-11
FP = 0.63 & b = 2.1	8.79E-09	3.32E-11

Table 5.1 - Mean and Standard Deviation of Photons
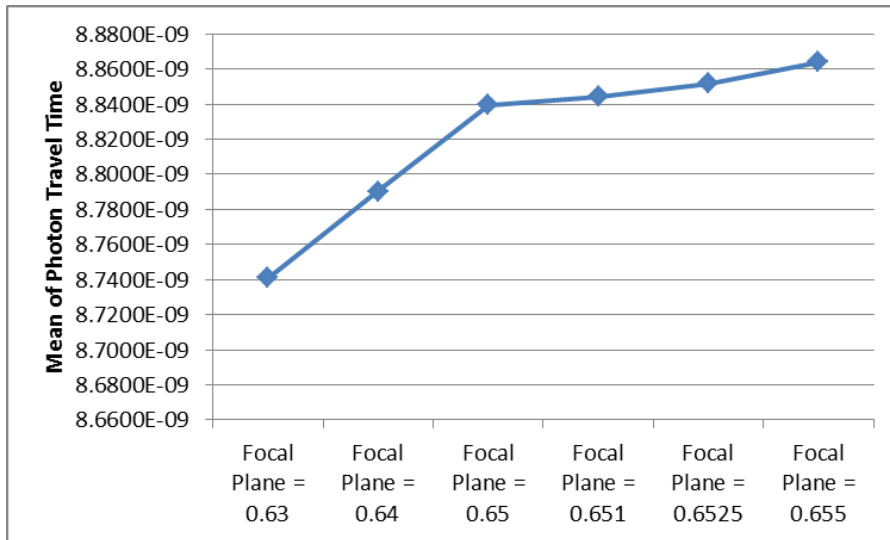
Figure 5.12 - Mean Photon Travel Time versus Focal Length
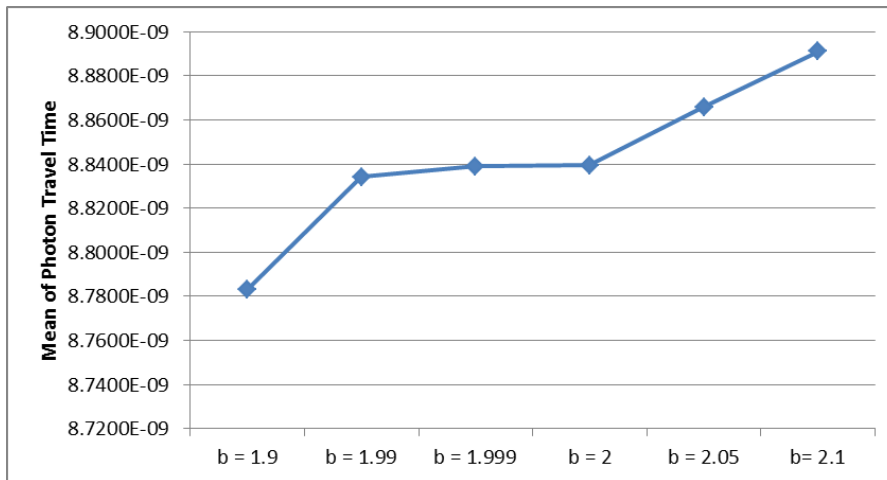
Figure 5.13 - Mean Photon Travel Time versus Surface Shape

By examining Figures 5.12 and 5.13 it is evident that there exists a direct correlation of structural and focal perturbation to the statistical variation in the photon arrival times. Varying the focal length of the model as in Figure 5.8, gave insight into the extent of the photon intensity distribution at the focal plane.   Upon inspection of Figure 5.11, the **b** parameter surface shape changes of the parabola imply the symmetric nature of the detector outputs of modeling b = 1.9 and 2.1, and the highest concentration of photons with the b = 2 parameter for a perfect parabolic surface.

Table 5.11, Figure 5.12, and Figure 5.13 describe the extent that which perturbing a parabolic focal system can have an effect on the statistics of photons being counted at a given detector. The largest deviation of the mean of the statistics maps directly to the greatest change in surface shape or focal plane distance. Simulating a perfect parabolic focal instrument was used as a baseline for the model verification. It has been shown that an analysis tool has been developed and verified for this parabolic focal system.

64

5.9 Defining a Parabolic Surface

An initial step is to mathematically model a representative parabolic surface to confirm the ray tracing algorithm. With x and y axis having an orientation as in Figure 5.9 and the z axis will be in the direction of the incoming light. The shape of the parabola is defined as in Eq. 5.8 for the preliminary confirmation of the simulation code. Advancing the research to a more realistic model required the integration of multiple software platforms and computational code.

Applying the FEA nodal displacement output to define a parabolic surface became an intricate threefold process:

1) Build the geometry of the parabolic dish including thickness, material, boundary conditions, and loads.
2) Run the FEA iterative solver in Solidworks for the total nodal displacements of a static analysis. Next, the original surface node positions (x,y,z) with the displaced positions ($\triangle$x,$\triangle$y,$\triangle$z) are exported and combined in Excel^{tm} .
3) With the displaced nodal values (x',y',z') make a new meshed surface using pointCloud2mesh.m Matlab software that uses Delaunay triangulation methods to mesh a surface with the number of triangulated surface elements, vertices, and normal vector of each element.

5.10 Convergence Study

Expanding the simulation complexity required the introduction of a 3-dimensional reflective surface. Globally the FEA unperturbed parabolic dish model is meshed throughout its volume. An option in the FEA modeler allowed for just the nodes at the

65

reflective surface to be exported. The 3-dimensional nodal cloud of points that was exported was then converted into a triangulated mesh of surface elements with Matlab code. This surface import into the ray tracing algorithm required refining the amount of reflective surface elements that make up the parabolic dish. A coarse mesh of surface elements discretizes the reflective dish into a small amount of surface elements which would not attain the accuracy needed for the ray tracing analysis. The mesh is made up of triangular surface elements that define the surface as in Figure 5.14.
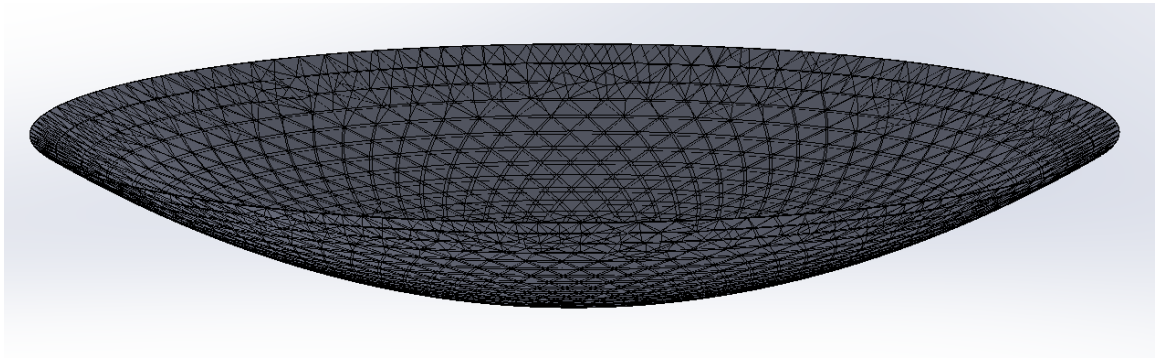
Figure 5.14 - Coarsely meshed FEA model

A gradual refinement of the surface elements into smaller triangular elements making up the reflective dish began to more accurately define the parabolic surface. A limit was established to the amount of surface nodes due to computational power. Firstly, the increased density of FEA elements increased the amount of computational time required for solving the nodal displacement values of the perturbed models. Secondly, the increased number of surface elements extends the computational time for the ray tracing algorithm to complete. The ray tracing algorithm required that every photon ray would need to find which triangulated surface it would reflect off of. The ray tracing

computational algorithm needed limits on the number of photons used in the simulation as well as the refinement of surface nodes (Figure 5.15).
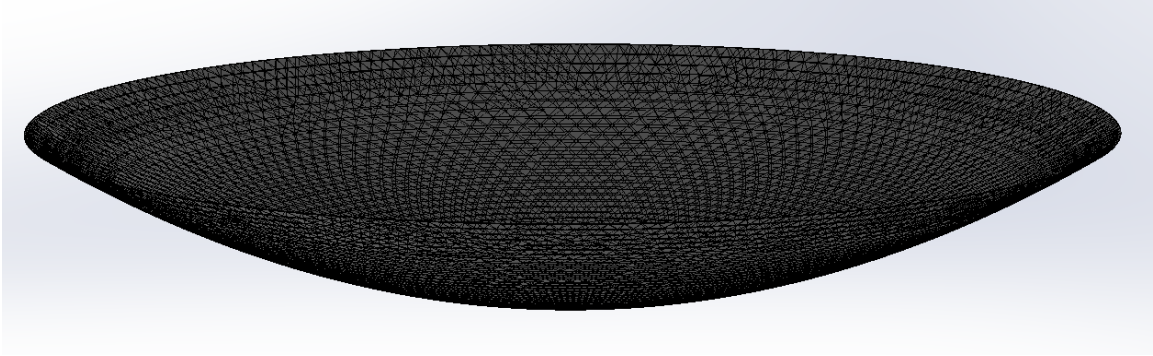
Figure 5.15 - Finely meshed FEA model
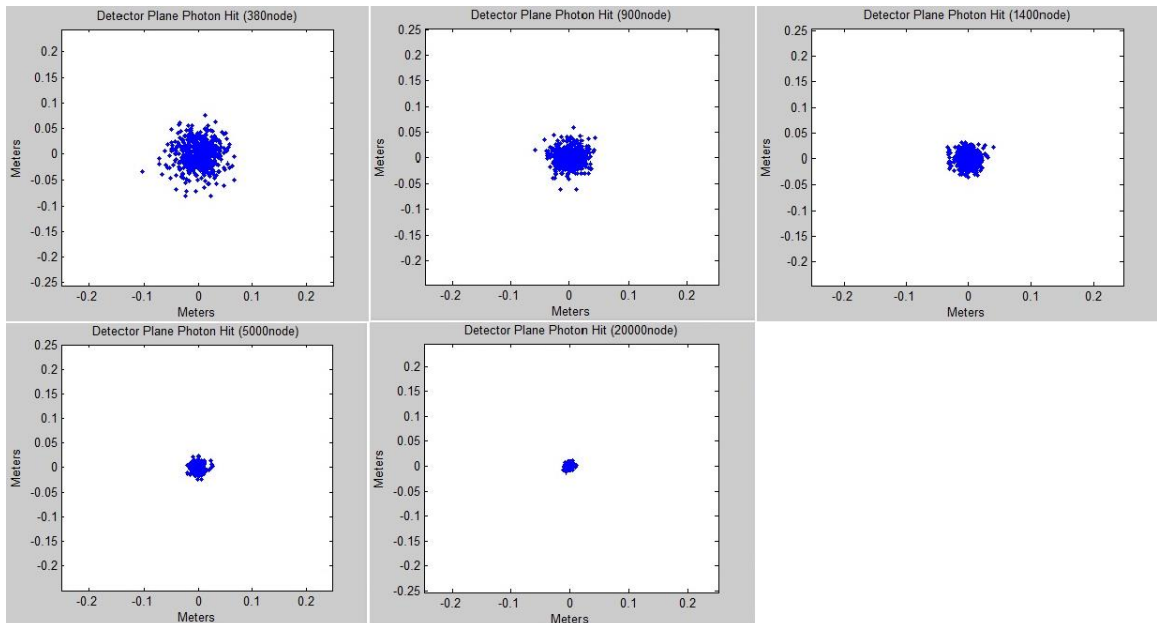
Figure 5.16 - Converging focal point with increased surface nodes

As can be seen in Figure 5.16 that increasing the number of triangulated surface nodes does indeed increase the focusing ability of the parabolic dish model. Figure 5.16,

illustrates how a coarse mesh produces a spot diagram that extends out from the focal plane center greater than ~200 cm² (top left). As the mesh is refined the spot diagram decreases to 12 cm², which was deemed acceptable for all the incoming light based on the original optical II (16 cm²) [2].

Nodes	376	900	1400	5000	20000
Photon #	Mean Distance(m)	Mean Distance(m)	Mean Distance(m)	Mean Distance(m)	Mean Distance(m)
1000	2.6470	2.6494	2.6495	2.6500	2.6500
5000	2.6442	2.6480	2.6482	2.6498	2.6500
10000	2.6446	2.6478	2.6489	2.6492	2.6500
15000	2.6449	2.6484	2.6484	2.6498	2.6500
20000	2.6452	2.6483	2.6493	2.6500	2.6500

Table 5.2 - Photon Number versus Surface Node Number

By evaluating Table 5.2, it was determined that ~20,000 nodes (~40,000 surface elements) and ~1000 photons for the simulation would exemplify the ray tracing physics and surface deformation shapes.

5.11 Perturbed Ray Tracing and Photon Statistics

The results of changing the shape of the parabolic dish mathematically has been explained and verified. Furthering the algorithm involves establishing a test matrix of simulation runs and the varying loading and boundary conditions for the imported FEA displaced models. As can be seen in Figure 5.17, changing the shape of the parabolic

reflecting dish changes the angle that the ray is reflected through the ray tracing model. The plane displacement is the primary variable to changing a given photons path travel length. Additionally, the change in angle gives another contribution to the photon travel length as the photon will not hit the focal point but an x-y displacement at the focal plane.
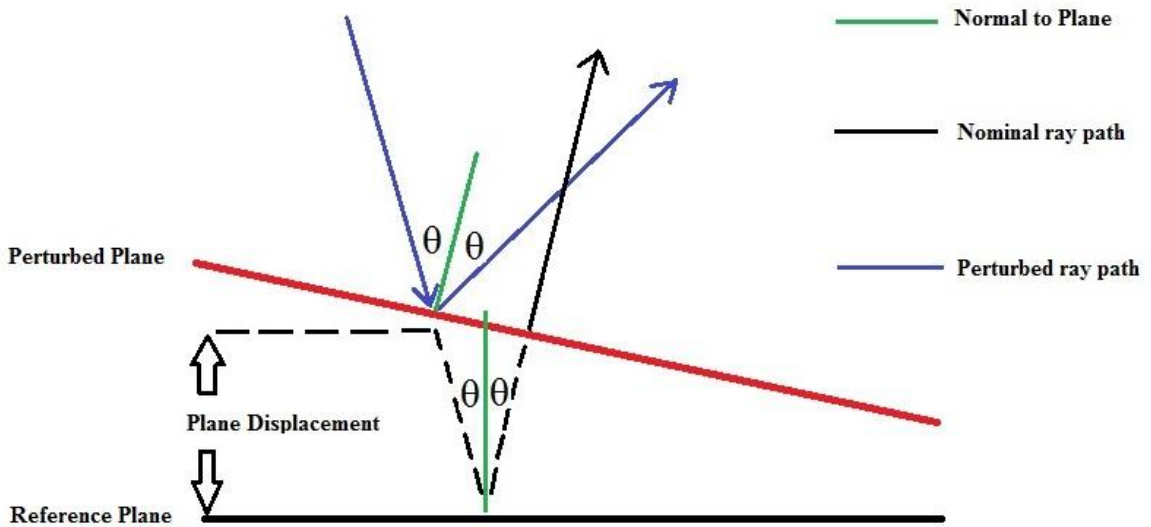
Figure 5.17 - Light ray path change with surface perturbation

Changing the shape of the reflective surface changes the path length which in turns changes the time that the photon travels through the focal system. The stochastic nature of how each photon enters the aperture will equate to a different path length change depending on where it reflects off of the distorted surface of the dish. Figure 5.18 illustrates the photon changes vector path lengths that contribute to the change in the correlation (similarity) measurement. For the gravity acting along the focal axis (Figures 5.20, 5.22, and 5.24), photons reflecting off the surface near the fixed rim will have minimal path length changes and the photons reflecting near the vertex will have a maximal change (focal/power

aberrations). The total path length change is both due to a contribution from aperture to the perturbed surface, after the reflection of the (un)perturbed surface (Figure 5.17), and the final component of path length change to where it hits on the detector plane. All of the path length components result in the path length vector change (Figure 5.18) which equated to when it is recorded in time at the focal plane. The read out times τ are equal to the total simulation time divided into a set of increments and can be related to the speed of a photo-sensitive detector.

Unperturbed Dish With High Correlation

Total Time/Deviations = Detector Time Intervals

| $\tau 1$ | $\tau 2$ | . | . |

Source Photon Stream

Detected Photon Stream

Deformed Dish With Low Correlation

Total Time/Deviations = Detector Time Intervals

| $\tau 1$ | $\tau 2$ | . | . |

Source Photon Stream

Detected Photon Stream

Path Length
Change Vectors

Resultant Photon
Stream Path Length
Change
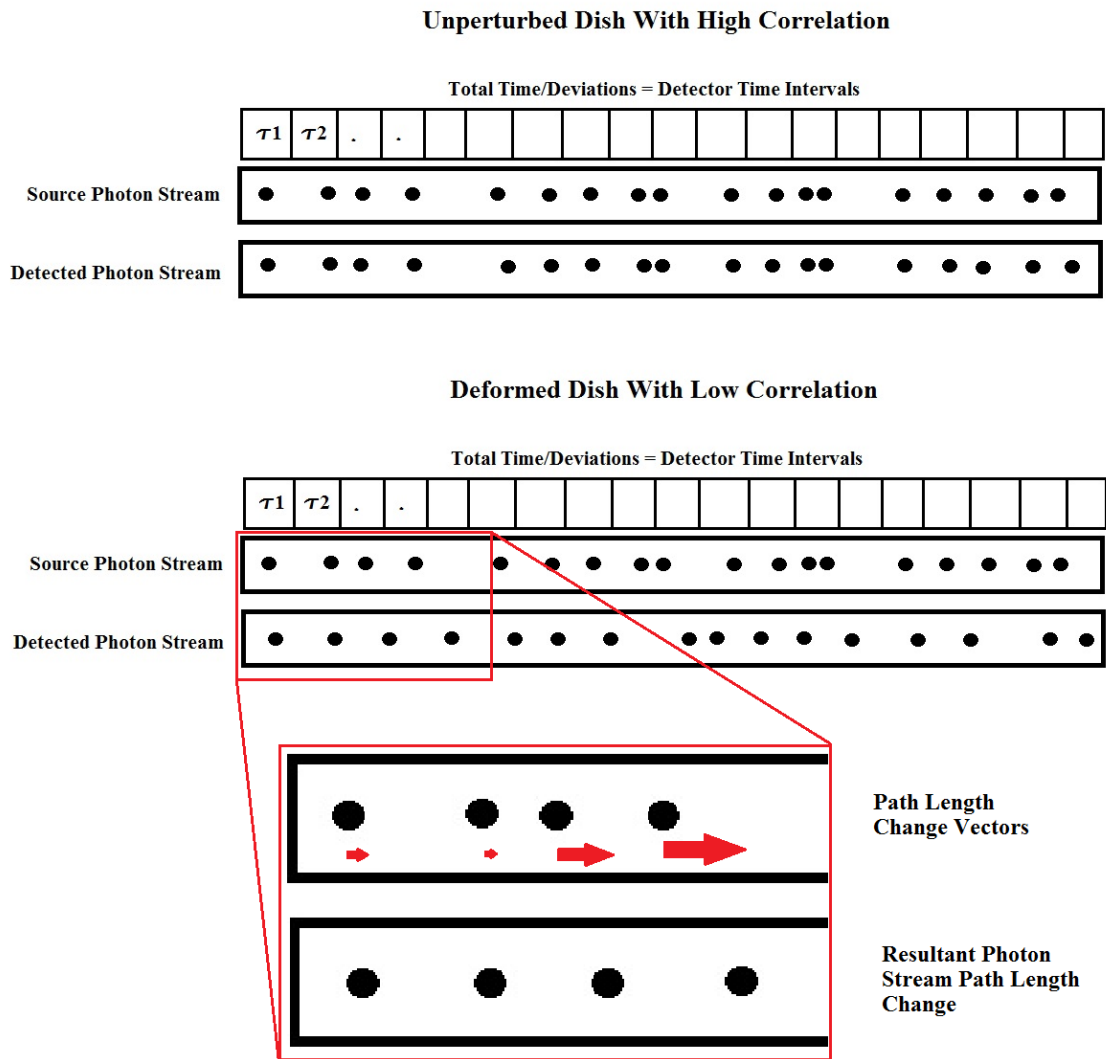
Figure 5.18 - Photon Correlation Measurement

70

The correlation measurement is the comparison of incoming source photon arrival times to that which is measured at the detector plane. This value is based on Equation 2.8, and used as a metric to define the statistical variation between two sets of photon streams. This measurement is also based on finite time increment of the averaging or the detector time intervals (Figure 5.18). The correlation value approaches a value of unity (Figure 5.19) as the time increment for averaging becomes larger and the correlation value approaches a minimum as the time averaging becomes smaller.
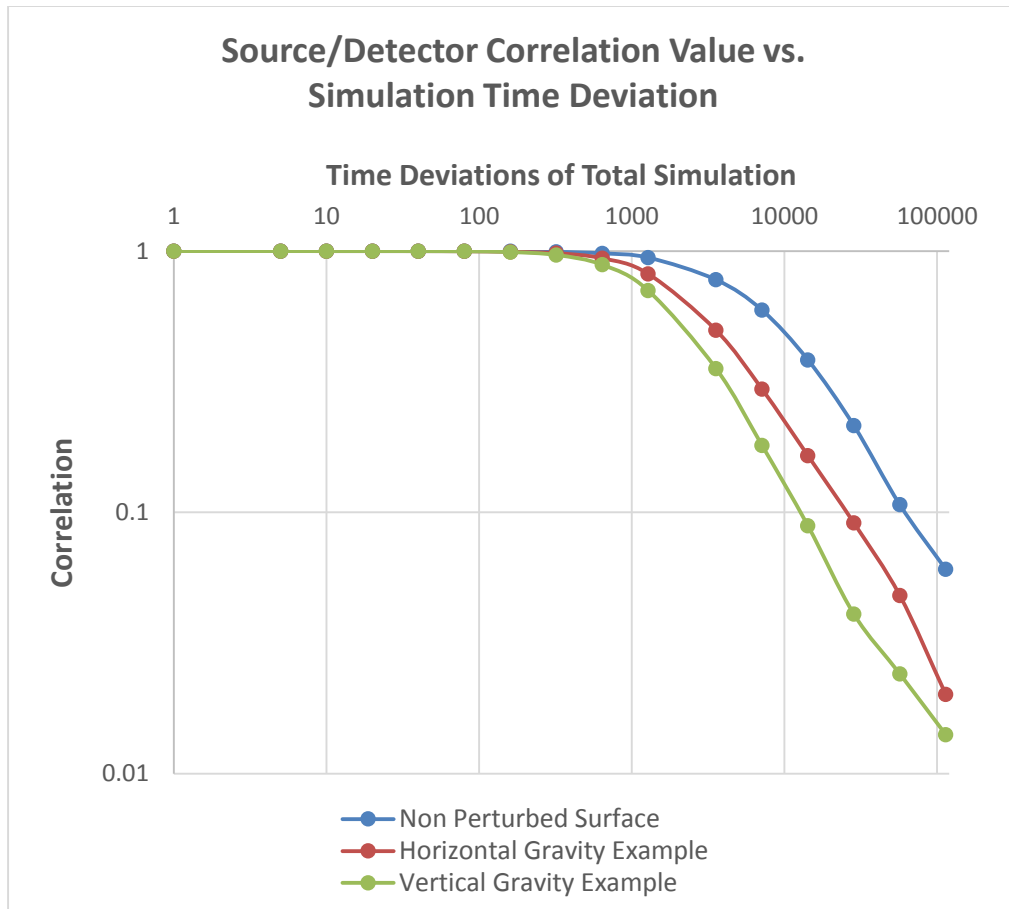
Figure 5.19 - Correlation Values Versus Simulation Time Deviation
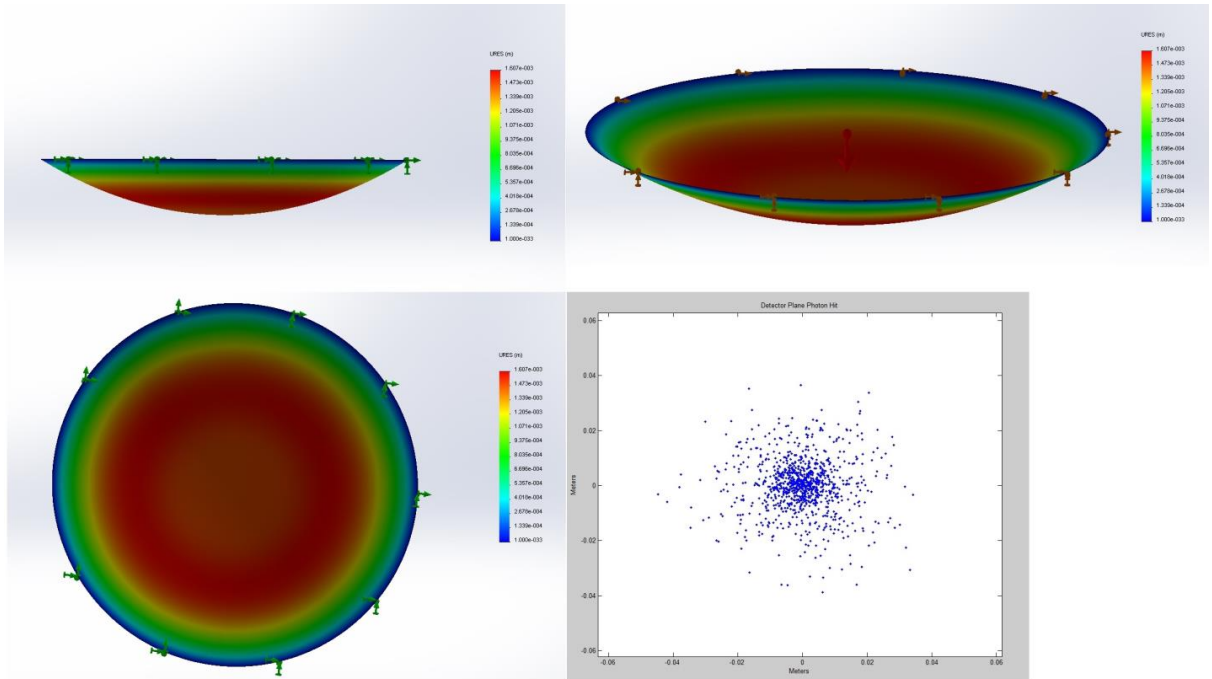
Figure 5.20 - 0.1mm Thick Horizontal Gravity Displacements/Focal Plane Photon Distribution, Maximum Resultant Displacement (Red) = 1.60mm
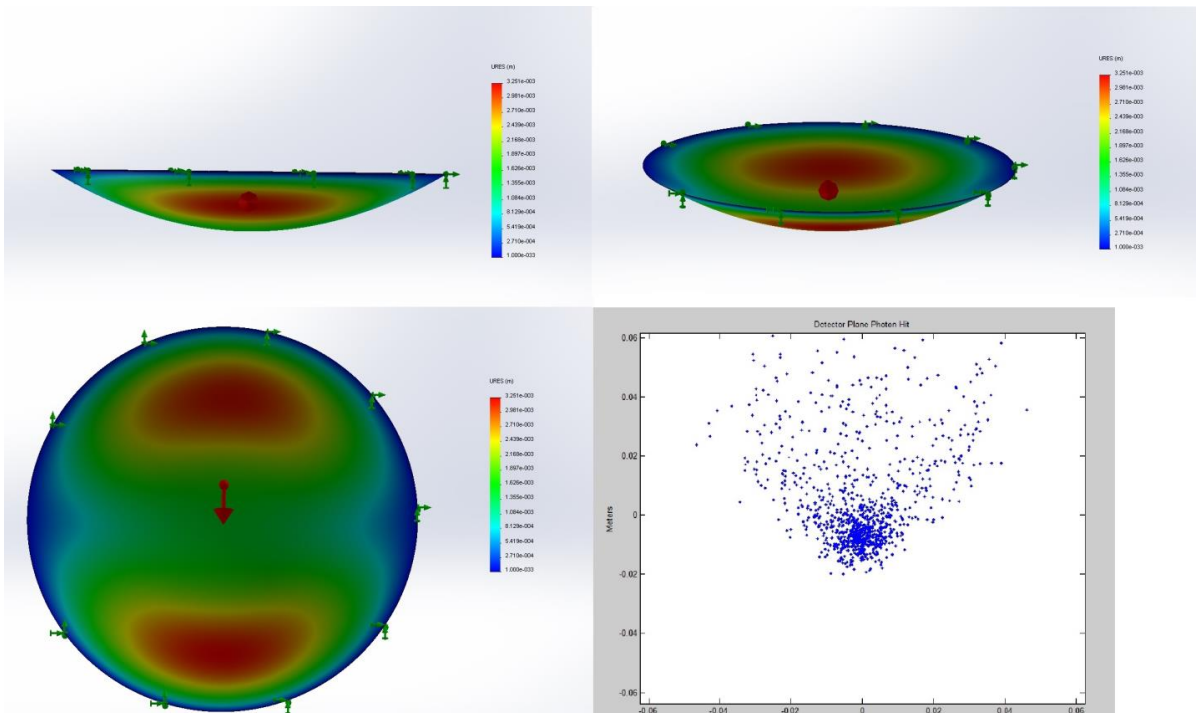
Figure 5.21 - 0.1mm Thick Vertical Gravity Displacements/Focal Plane Photon Distribution, Maximum Resultant Displacement (Red) = 3.25mm
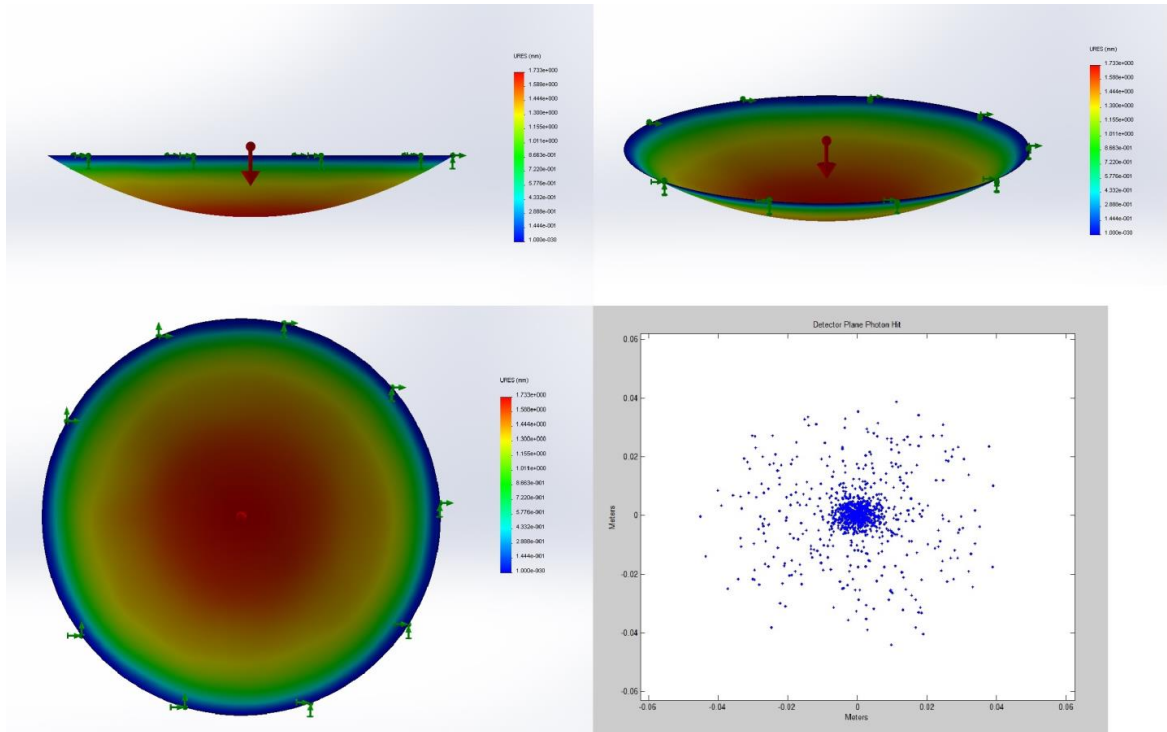
Figure 5.22 - 1mm Thick Horizontal Gravity Displacements/Focal Plane Photon
Distribution, Maximum Resultant Displacement (Red) = 1.73mm
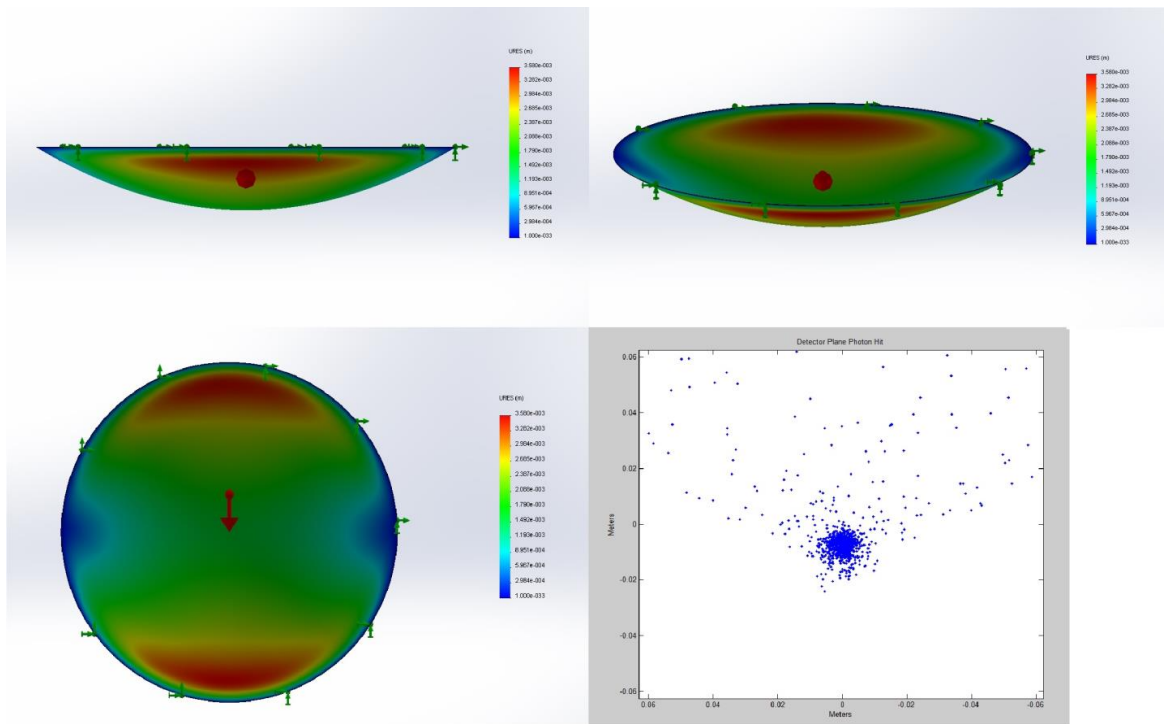
Figure 5.23 - 1mm Thick Vertical Gravity Displacements/Focal Plane Photon
Distribution, Maximum Resultant Displacement (Red) = 3.58mm
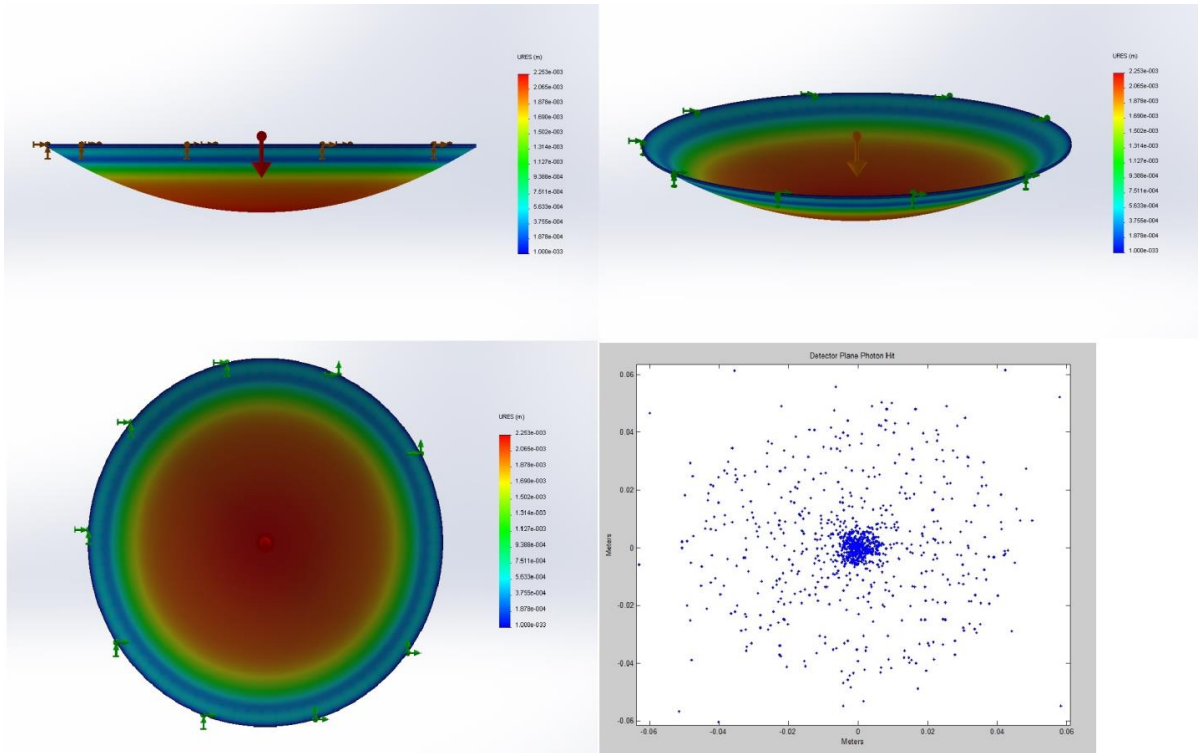
Figure 5.24 - 10mm Thick Horizontal Gravity Displacements/Focal Plane Photon Distribution, Maximum Resultant Displacement (Red) = 2.25mm
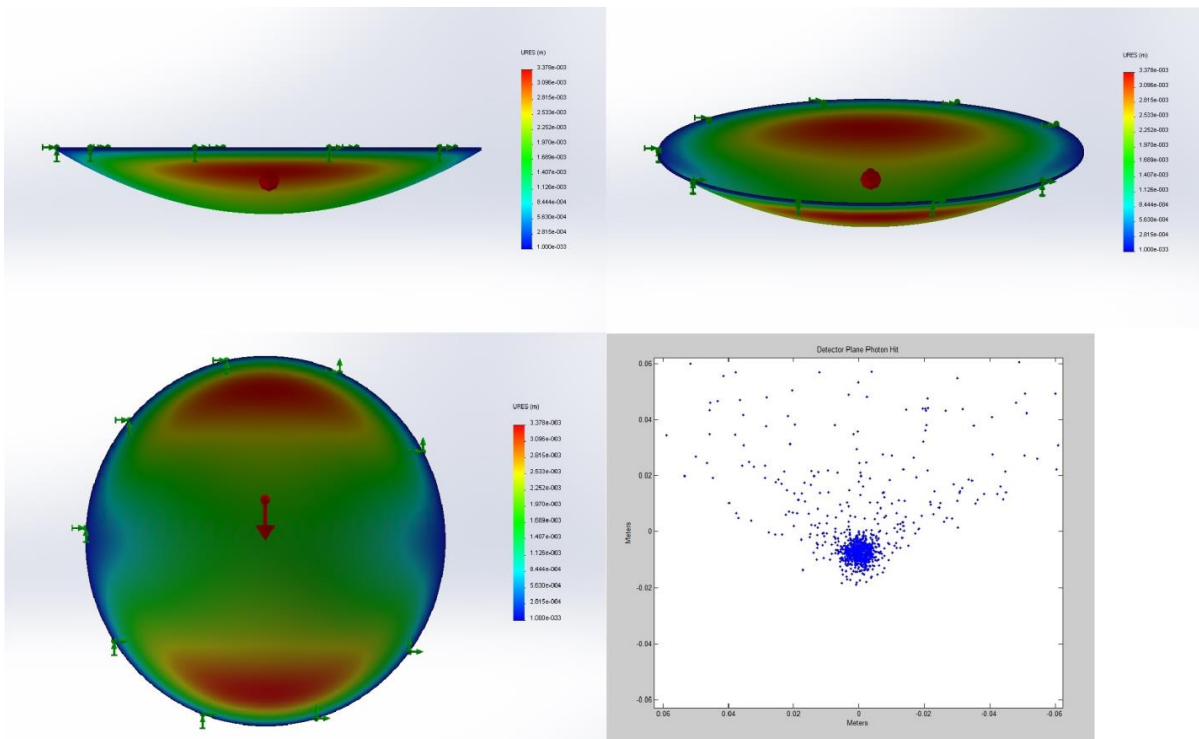
Figure 5.25 - 10mm Thick Vertical Gravity Displacements/Focal Plane Photon Distribution, Maximum Resultant Displacement (Red) = 3.38mm
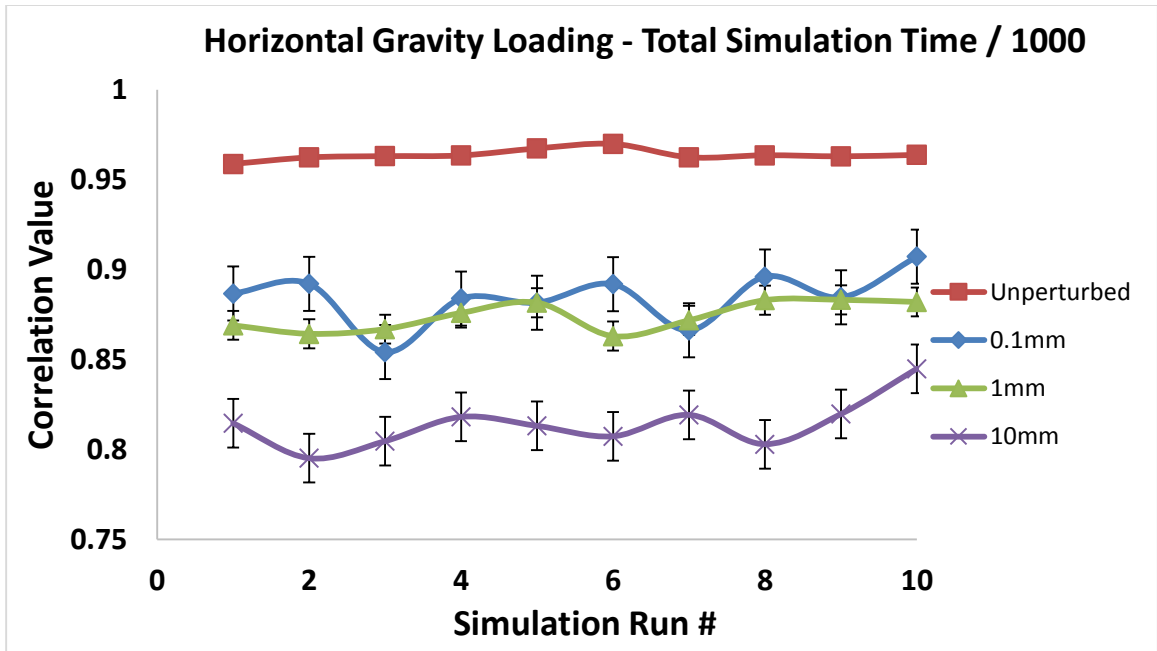
Figure 5.26 - Horizontal Gravity Loading (1000 Time Deviations)
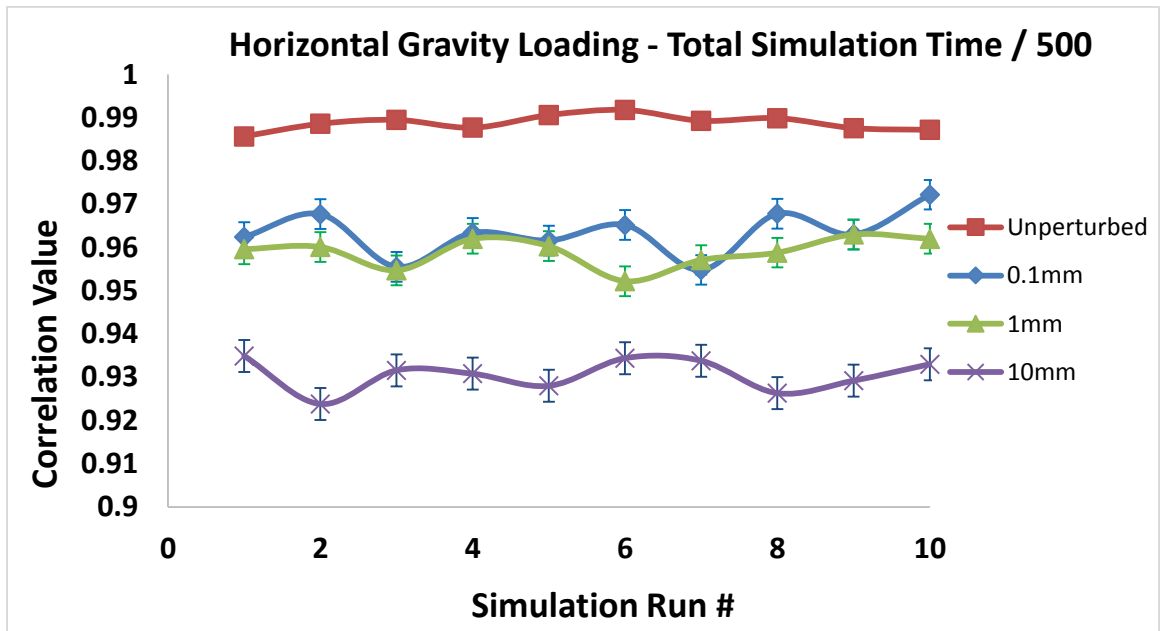
Figure 5.27 - Horizontal Gravity Loading (500 Time Deviations)
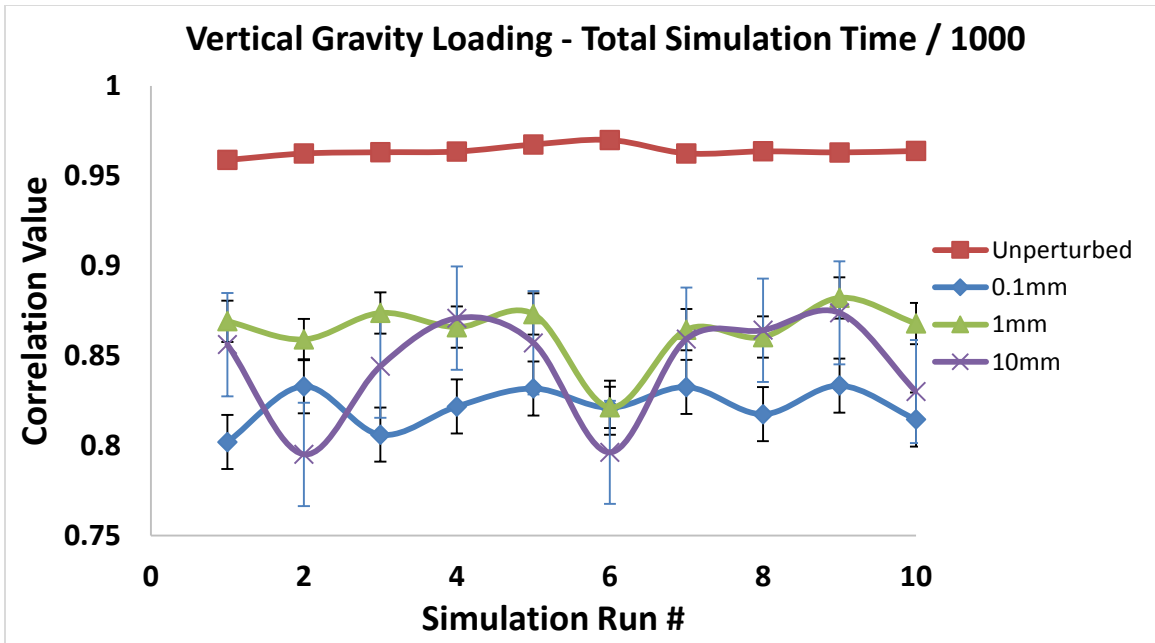
Figure 5.28 - Vertical Gravity Loading (1000 Time Deviations)
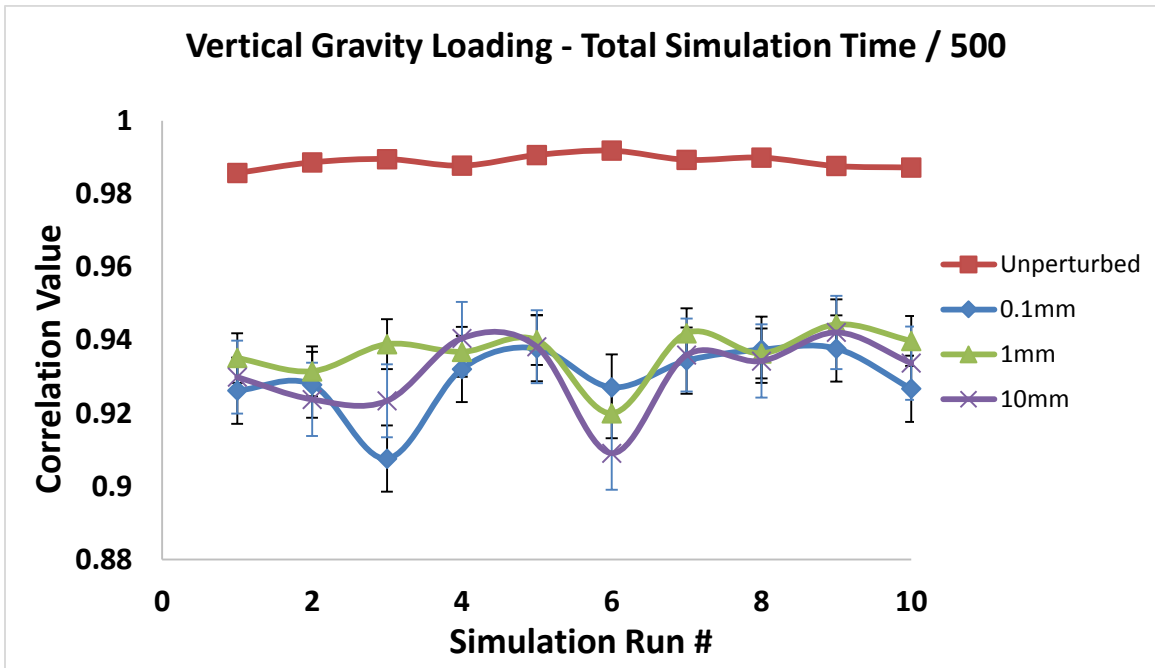
Figure 5.29 - Vertical Gravity Loading (500 Time Deviations)

Ten separate photon streams (k1 of Eq. 5.22) were applied to the II simulation algorithm. Each photon stream set $k1(1) - k1(10)$ interacted with both the unperturbed and deformed dish scenarios of Figures 5.20-5.25 where the error bars are based on the standard deviation of the mean for each data series. The unperturbed data provides a baseline for the horizontal gravity loading as in top (red) of Figures 5.26 and 5.27. There are similarities for both the 0.1mm and 1mm thickness correlation plots, this is directly related to the similarity in maximum displacements of 1.60mm and 1.73mm, respectively. An even greater loss in correlation values occurred for the 10mm thick parabolic dish with a maximum displacement of 2.25mm. The horizontal gravity loading scenarios (focus/power mirror aberrations) exhibit a distinct trend in their respective correlation values. Examining the bottom/left images of Figures 5.21, 5.23, and 5.25 describes the non-symmetric displacement surface result. Where the top (red) maximum displacement falls closer to the focal plane and the bottom (red) falls away from the focal plane (Figure 4.5). The vertical gravity loading scenarios (coma mirror aberrations) do exhibit a general loss in correlation values from the baseline values but vary more significantly than the horizontal cases. Due to the stochastic nature of the spatial and temporal contribution to the photon path length differences, the photon timing signatures change adding path length, as well as, take it away (red vectors would point in both directions in Figure. 5.18). It has been shown that the correlation measurement with the source and detected photon stream are affected by parabolic dish deformation. The second order correlation measurements conducted in the simulation runs do provide values that are coupled to the amount of deformation of the reflective dish. Interesting patterns emerge as can be seen in the vertical

gravity cases where the random nature of the Poisson distributed photon streams combine with more complex geometries of deformation.

5.12 Correlation Value Related to Resolution of Source

Understanding how the correlation value of an II instrument relates to its ability to resolve the size of the nearest stars was the primary measurement made in the original II experiments. Figure 2.1 describes how correlation values decrease with detector separation. The angular extent of the source directly relates to how much separation the II instrument detectors need to have in order to resolve the object. Equation 5.23 [2] is the relationship of correlation values, $C(d)$, and the baseline separation between two detectors, d. This correlation value is based on the beat frequencies derived in Appendix A. The constant K will be a value equal to 1 when each detector is receiving and processing the same amount of radiation from a given source. λ is the mean wavelength of light and θ is the angular separation of two points on the distant source.

$$C(d) = K \; \cos \frac{2\pi d\theta}{\lambda} \qquad\qquad \text{[Eq. 5.23]}$$

The separation distance was assumed to have value of $d = 1$ for a correlation value $= 0$. The theoretical value of the correlation will be one when the detectors are at the same position (maximum beat frequency strength) and decrease to a value of zero (minimal beat frequency strength) when the detectors are separated to a point at which the two light emitting points are located at extremes on the source, producing a minimal correlation value, Figures 5.30 and 5.31. When the correlation is zero, the separation, d, of the

detectors can be plugged into Eq. 5.23 to solve for the angular separation of the two

source points.
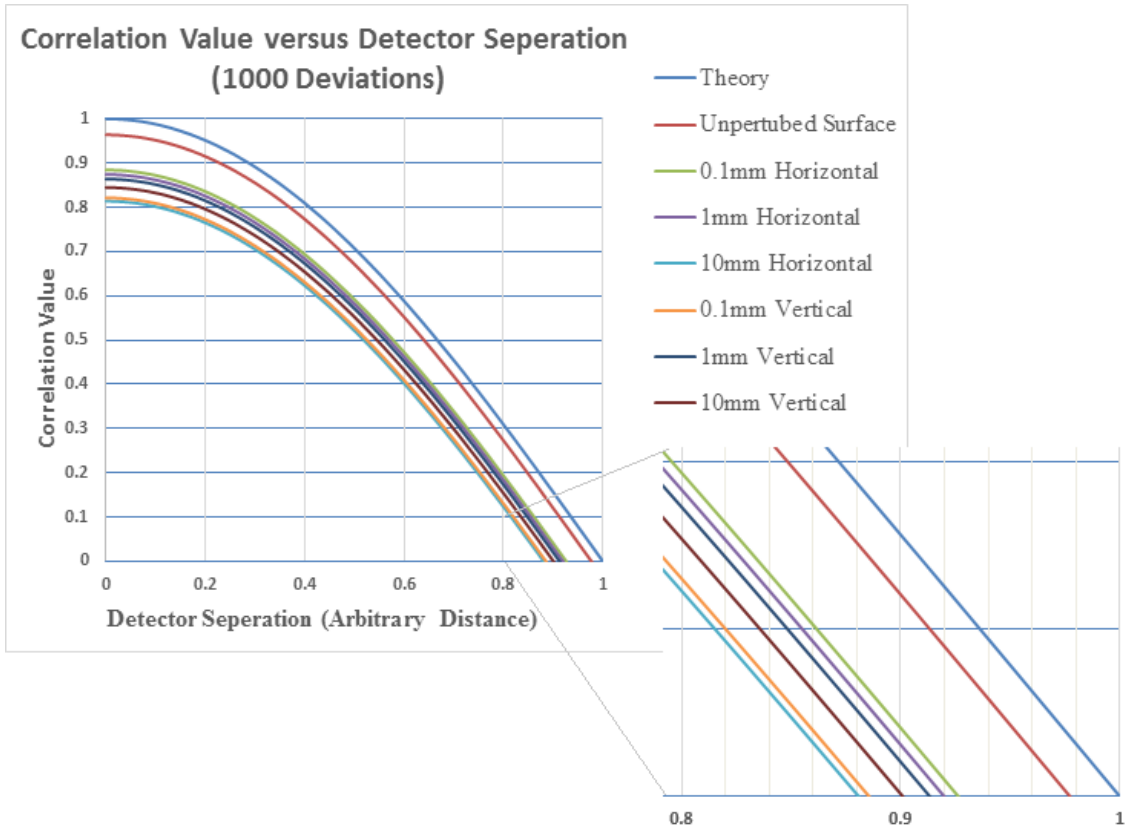
Figure 5.30 – Correlation versus Detector Separation (1000 Deviations)
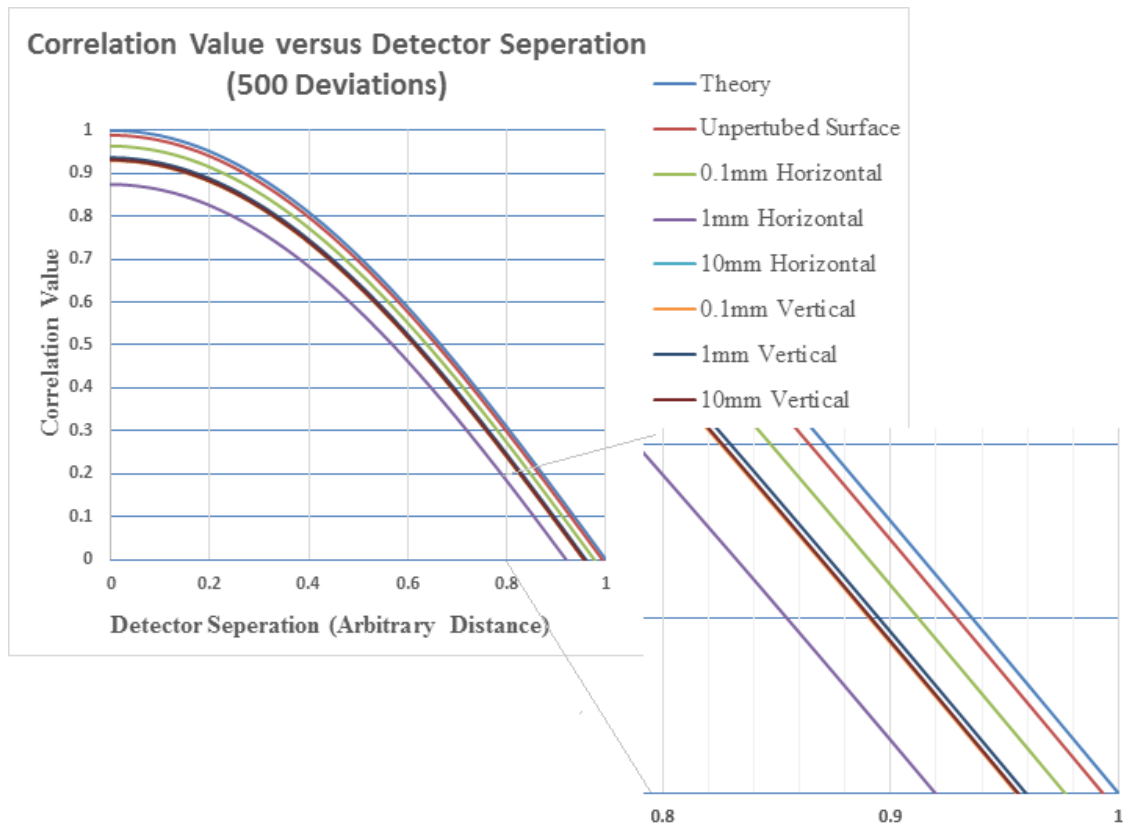
Figure 5.31 – Correlation versus Detector Separation (500 Deviations)

Discretizing the dish into a finite number of triangular surface elements (~40,000) introduced an error due to not completely representing a smooth surface of the reflecting parabolic mirror. Averaging the values of the correlation for the ten simulation runs, the red values of Figures 5.26 – 5.29, and plotting that average value scaled to the theoretical value of the correlation illustrates the extend that the surface discretization has on the correlation value.   This equated to about a correlation value = 0.989, a 1% error for the 500 deviated values, and a correlation value = 0.965, a ~3.5% error for the 1000 deviated values. This unperturbed dish correlation value versus detector separation is plotted in red near the theoretical (blue) value on the far right of Figures 5.30 and 5.31.

Figures 5.30 and 5.31 show the values obtained by using Eq. 5.23 for the all of the perturbed surfaces of both the horizontal and vertical gravity loads with the varying dish thicknesses, as well as, the unperturbed and theoretical values. The correlation versus detector separation was used as a comparison to exemplify the extent that a perturbed surface would have on a two detector II instrument. The data of importance is located in the lower right of Figures 5.30 and 5.31. This area of the plot shows how perturbed surfaces affect the accuracy of an II measurement. Comparing the data in Figures 5.26 - 5.29 illustrates that the 1000 deviated plot had a much larger spread of perturbed line values compared to the 500 deviated perturbed line values for both of the correlation versus detector separation plots. Figure 5.30 demonstrates the accuracy that an II instrument can resolve an object decreases by ~10% for the simulated time frames and dish perturbations. This reduction in resolution was evident in Figure 5.31 as well, with many of the plotted lines overlapping. All of the perturbed dish displacements lines approached a zero correlation point that was less than the unperturbed dish and theoretical values. The simulation setup and all of the simulation runs showed that a dish with a maximum displacement ranging from ~1- 4 mm reduces correlation and resolution values by 5-10%, assuming all other variables are fixed.

Chapter 6

Conclusions

An overview of Intensity Interferometry was provided. II is finding new applications in many aspects of science, especially in particle and astrophysics, due to advances in photo detectors and computational speeds. With the model and simulation set forth it was demonstrated that minimal parabolic deformations have a significant effect on the accuracy that an II measurement can attain. The effect of thickness and orientation of the telescope were studied and the results were evaluated.

A multi-tiered simulation was performed to extract the significance of how gravitation loading can effect a parabolic shell. It was verified that the shape of the perturbed reflector can have profound effects on the photon statistics that are fundamental to an Intensity Interferometric measurement. The analysis involved varying the thickness of the parabolic shell, applying fixed rim boundary conditions, and gravitational body force loading on two different axial components. It has been demonstrated that the structural and focusing deformations of a parabolic focal system have a quantifiable effect on the statistics of photon streams impinging on a focal plane. Redundant simulation runs were performed to build up confidence for each perturbed reflective surface scenario. The final results for the simulated II telescope confirmed a loss off second order correlation value for the deformed surface shapes as compared to the pristine parabolic reflector dish. A comparison of correlation values versus detector separation was also performed describing how perturbed parabolic dishes reduce resolution limits for a two detector II instrument.

The future of this work will include modeling the monochromatic light with a greater precision and developing original photon statistical analysis to include expounding on the number of surface shapes for reflecting parabola/detector systems. Higher order aberrations can also be applied to the simulation tool to give greater insights as has been conducted with traditional telescopic imaging mirrors. Additional research will also introduce detector noise, photon detector/reflection loses, and correlation of multiple focal systems to define structural effects on intensity interferometry.

As technology advances with changes to specific instrument components such as photon detectors other technical aspects of a complete instrument must also be addressed. Scientific studies that involve large optical structures to collect light are needing further and more refined analysis. Addressing how structural influences effect scientific measurement on the shortest of timescales will become paramount. Mixing multiple software platforms and basic mathematics, such as the simulation algorithm of this dissertation, is a driving example of how many refined tools can be combined to extract novel engineering methods for discovering unexplored areas of physics. This dissertation established an algorithm technique that is not only cost effective (no physical experimentation), but also has repeatable results with analytical confirmations.

References:

[1] **F. Millour., All you ever wanted to know about optical long baseline stellar interferometry, but were to shy to ask your advisor, Max-Planck Institute for Radio Astronomy (2008)**

[2] **R. Hanbury Brown., The Intensity Interferometer, Halsted Press-New York (1974)**

[3] **R. Holmes, C. Brandoch., Cramer-Rao Bounds for Intensity Interferometry Measurements, Applied Optics, Vol 52 (2013)**

[4] **P. Crabtree, J. Murray-Krezan, R. Picard., A Study of Image Reconstruction Algorithms for Hybrid Intensity Interferometers, SPIE Vol. 8165, 2011.**

[5] **C. Wong., Intensity Interferometry for a Chaotic Source with a Collective flow and Multiple Scattering, J. Phys. G 29 (2003)**

[6] **P. Fontana, Multidetector Intensity Interferometers., J. Appl. Phys 54 (1983)**

[7] **O. Aviv, E. Ribak, Offline, Multidetector Intensity Interferometry-I. Theory., Mon. Not. R. Astron Soc. 368 (2006)**

[8] **P. Nunez, Towards Optical Intensity Interferometry for High Angular Resolution Stellar Astrophysics, University of Utah (2012)**

[9] **V. Herrero, Design of Optical Telescope Arrays for Intensity Interferometry, Astronomical Journal. Vol 76 (1971)**

[10] **I. Klein, M. Guelman, Space-Based Intensity Interferometry, Optical Society of America (2007)**

[11] **D. Gerwe, P. Crabtree, Image Reconstruction from Sparse Irregular Intensity Interferometry Measurements of Fourier Magnitude, Air Force Contract FA9453-12-C-0129**

[12] **C. Pellizzari, R. Holmes, Intensity Interferometry Experiments and Simulations, Proc. of SPIE, Vol 8520 (2012)**

[13] **S. Sattler, H J Hartfuss, Intensity Interferometry for Measurement of Electron Temperature Fluctuations in Fusion Plasmas, Plasma Physics, Control, Fusion, Vol 35 (1993)**

[14] **H. Lajunen, V. Torres, Resolution-Enhanced Optical Coherence Tomography based on Classical Intensity Interferometry, J. Opt. Soc. Am. A, Vol.26 (2009)**

[15] **D.Hyland, Exo-planet detection via stellar intensity correlation interferometry, SPIE Vol 5905 (2005)**

[16] **O. Aviv, E. Ribak, Micro-arcsec imaging from the ground with intensity interferometers, European Interferometry Intitiative (2005)**

[17] **D.Dravins, Astrophysics on its Shortest Timescales, www.eso.org/sci/publications/messenger/archive/no.78-dec94/messenger-no78-9-19.pdf**

[18] **C. Foellmi., Intensity interferometry and the second-order correlation function g(2) in astrophysics, A&A 507, 1719-1927(2009)**

[19] **Rotondo, F., Imaging with Amplitude and Intensity Interferometers, Institute for Defense Analyses (2004)**

[20] **D. Dravins, S. LeBohec., Towards a diffraction-limited square-kilometer optical telescope: Digital revival of intensity interferometry, SPIE (2008)**

[21] **C. Dimarzio, Optics for Engineers, CRC Press Boca Raton, Florida (2012)**

[22] **E. Wolf, Introduction to the Theory of Coherence and Polarization of Light, University Press Cambridge (2007)**

[23] **H. Young, Statistical Treatment of Experimental Data, McGraw-Hill (1962)**

[24] **R. Loudon, The quantum theory of light, Oxford University Press, Oxford (2000)**

[25] **L. Mandel, J. Opt. Soc. Amer. 51 (1961)**

[26] **M. Facao, A. Lopes, A. L. Silva, and P. Silva, Computer simulation for calculating the second -order correlation function of classical and quantum light. Eur.J.Phys Vol 32 (2011)**

[27] **M. Hiroshi, Requirements on Photon Counting Detectors for Terahertz Interferometry. J Low Temp Phys (2012).**

[28] **S.Cova, M.Ghioni, A.Lotito, I.Rech, and F.Zappa. Evolution and prospects for single-photon avalanche diodes and quenching circuits. J.Mod.Opt, Vol 51 (2004)**

[29] **D.Dravin, C. Barbieri, R.A.E. Fosbury, et al. QuantEYE: The Quantum Optics Instrument for OWL. Paper proceedings of IELT, (2005)**

[30] **G. Vannucci, M. Carl Teich, Computer simulation of superposed coherent and chaotic radiation, Applied Optics. Vol 19 (1980)**

[31] **F. Jin, H. DeRaedt, and K. Michielsen, Event-by-event simulation of the Hanbury Brown-Twiss experiment with coherent light. arXiv:0908.1040V1 Q (2009).**

[32] **J. Rou, Monte-Carlo Simulation of Stellar Intensity Interferometry. Senior Thesis, The University of Utah (2012).**

[33] **C. Pellizzari, R. Holms, and K. Knox, Intensity interferometry experiments and simulations. SPIE Vol 8520 (2012)**

[34] **D. Gerwe, J.J. Dolne, P. Crabtree. Image Reconstruction from Sparse Irregular Intensity Interferometry Measurements of Fourier Magnitude. Proceedings of the Advanced Maui Optical and Space Surveillance Technologies Conference (2013)**

[35] **I. Klein, M. Guelman, Space-Based Intensity Interferometry, Optical Society of America (2007)**

[36] **M. Coleman, F Baginski, Modeling the Shape of Deployable Large Aperture Antennas in Non-Symmetric Loading Enviornments, AIAA Student Region MA-I Conference (2009).**

[37] **Lemaitre G. N., "Astronomical Optics and Elasticity Theory", Springer, ISBN# 978-3-540-68904-1, pp 423-440 (2009)**

[38] **Timoshenko S. and Woinowsky-Kreiger S., "Theory of Plates and Shells", McGraw-Hill, ISBN# 0-07-064779-8, pp. 433-436, 445-447 (1987).**

[39] **Physics Lectures Winter (2009)**
http://scipp.ucsc.edu/~haber/ph5B/parabolic09.pdf

[40] **Ajmal Saeed Mian., PointCloud2mesh.m - Matlab[tm] file, Computer Science Department, University of Western Australia (2012)**

Appendix A

Correlation techniques begin with understanding the interference output of detectors separated in time and space. Figure A.1 shows the most basic intensity interferometer with two receivers, A and B which can be defined as two photodetectors that convert nearly monochromatic photonic energy to output currents i_1, i_2. These currents are fluctuating in time and the currents are combined together in a combiner/correlator where the information is then multiplied together. The two output currents entering the combiner can have similar currents at the same time and will result in a "correlation" of the photonic detections. There are two types of photocurrent generated in these types of detectors. One is called shot current and is associated with a finite number of particles that transport energy with a random nature. The second type of current is called wave noise which is due to the fluctuations of the intensity of the light waves.
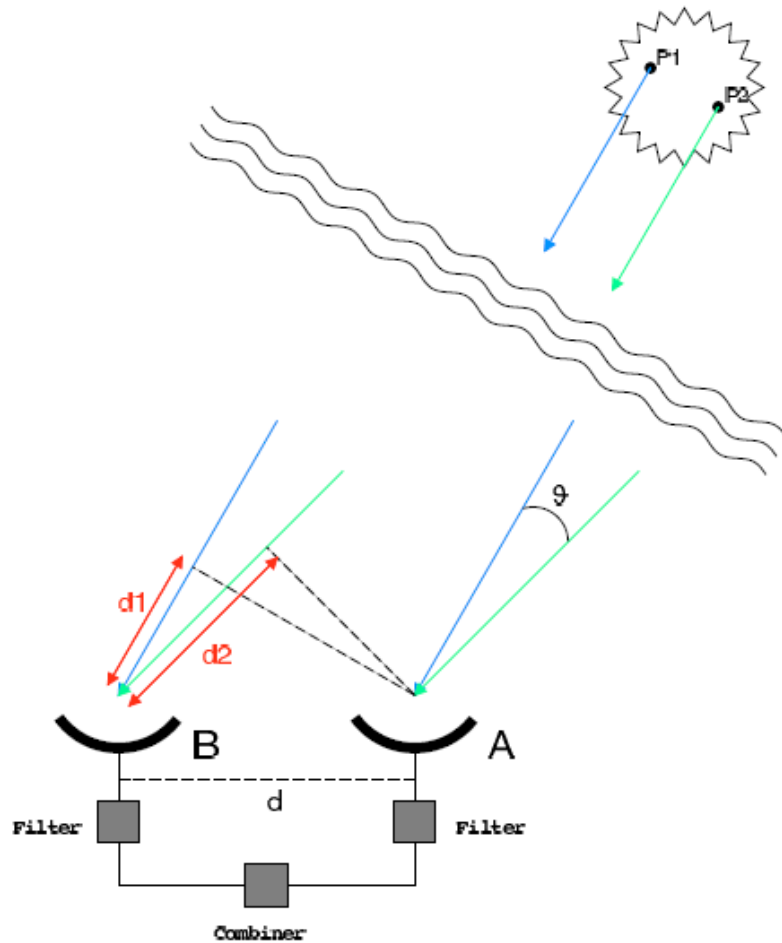
Figure A.1 [5]

An essential step is to subtract out the erroneous information that does not contribute to the actual correlation measurement. Shot noise (random photon generation due to electrical and thermal noise in the detection system) can easily be suppressed because one of the detectors shot noise will typically not have the same values as the second detector. Thus their different photocurrents can eventually be subtracted out before entering the correlator algorithm. However, the wave noise measured in one detector will have some degree of correlation to that measured in the other detector and these two similar currents can be combined in a linear multiplier. By defining the fluctuations of the two currents as $\Delta i_A(t)$ and $\Delta i_B(t)$, we can calculate the degree of coherence as:

$$c_n(d)/c_n(0) = < \Delta iA(t)\Delta iB(t) > /(< iA >< iB >) = |\gamma_d|^2 = V_d^2 \qquad [1]$$

Where $|\gamma_d|^2$ is the degree of coherence, V_d is a similar term to the fringe visibility in a Michelson interferometer setup, $c_n(d)$ component is a normalized correlation term with a baseline d, and $c_n(0)$ is a correlation factor related to the characteristics of the instrument.

The first step in evaluating the correlations between pairs of point sources is to start with a Fourier description of the energy from each point P_1 and P_2 reaching a specific detector but also incorporating the randomness of the amplitude and phase compared to the other component.

$$C_1 = E_1(\omega_1\tau + \phi_1) \qquad [2]$$

$$C_2 = E_2(\omega_2\tau + \phi_2) \qquad [3]$$

E is the electromagnetic field amplitude, ω is the frequency, and ϕ is the phase. The radiation is turned into electrical currents within the photo detectors and is proportional to the arriving intensity [2]. The resulting current at detector A is:

$$i_A = K_A[E_1 \sin(\omega_1 t + \phi_1) + E_2\sin(\omega_2 t + \phi_2)]^2 \qquad [4]$$

A similar Fourier component will reach detector B but with the added terms of d_1 and d_2 as depicted in Fig A.1. This results in a modified version of equation 4:

$$i_B = K_B[E_1 \sin(\omega_1(t+d_1/c)+\phi_1) + E_2\sin(\omega_2(t+d_2/c)+\phi_2)]^2 \qquad [5]$$

Expanding both of these terms [Eq 5,6] by evaluating the square leads to two terms which are the sum of the light intensities from both components, and a term that is the intensity of the sum of the different frequencies ω_1 an ω_2:

$$i_A = \frac{1}{2}K_A\{(E_1^2 + E_2^2) - [E_1^2 \cos 2(\omega_1 t + \phi_1) + E_2^2 \cos 2(\omega_2 t + \phi_2)]$$
$$- 2E_1E_2 \cos[(\omega_1 + \omega_2)t + (\phi_1 + \phi_2)] + 2E_1E_2 \cos[(\omega_1 - \omega_2)t + (\phi_1 - \phi_2)]\} \qquad [6]$$

$$i_B = \frac{1}{2}K_B\{(E_1^2 + E_2^2) - [E_1^2 \cos 2(\omega_1(t+d_1/c)+\phi_1) + E_2^2 \cos 2(\omega_2(t+d_2/c)+\phi_2)]$$
$$- 2E_1E_2 \cos[(\omega_1 + \omega_2)t + \omega_1 d_1/c + \omega_2 d_2/c + (\phi_1 + \phi_2))$$
$$+ 2E_1E_2 \cos[(\omega_1 - \omega_2)t + \omega_1 d_1/c - \omega_2 d_2/c + (\phi_1 - \phi_2))\} \qquad [7]$$

Each term represents a different component in the final measurement. The first term in each equation is the total amount of light flux reaching the detector. The second and third terms are representative of the second harmonics which is typically subtracted out with appropriate filters. The final term with the difference of the frequencies *(ω1 - ω2)* is the one that is essentially what Hanbury Brown & Twiss (1957) had discovered as being the term that corresponds to the measured beat frequency. The fundamental point is that the correlation of the two intensity fields is a function of the difference in phase between the low frequency beats formed at the two detectors [2].

Appendix B

II Simulation

```
%Mark Harris 1/1/5/14 PhD Dissertation Research
%code for an intensity interferometer(II) instrument
%This simulation is designed to simulate far field photons
%traversing a focal reflecting II instrument and be received
%at a detector surface (units are in m)
%Allocate rate and number of photons being emitted from a distance
source
%Initialize variables
%Add travel time of photon through simulated instrument to detector
%located at the focal point.
%Load data(xyz nodal pts) triangles.mat and vertices.mat in workspace

n = 2000;   %Number of possible emission states
dradius = .78; %radius of airy disk and original parabola in meters
x1 = zeros(n,1); %column of zeros for original x values
y1 = zeros(n,1); %column of zeros for original y values

%Step1 - Define a Poission distribution of 1 and 0's Frequency
% [1xn] matrix  1 represents an emission of a photon, 0 is null.
% this code generated a poissionian number distribution of 1 and zero's
% with median 0.5 to increase the mean decrease the trailing term.

t1 = rand(n,1).*sign(rand(n,1) - .5);   %k1 is inserted manually
for i = 1:n
    if t1(i) >= 0;
        k1(i) = 1;
    else if t1(i) < 0;
            k1(i) = 0;
        end
    end
end
% t2 = rand(n,1).*sign(rand(n,1) - .5);   %k1 is inserted manually
% k1sim = k1;
% Step2 - generate evenly distributed points on photon emission disk
% n = number of iterations
% dradius = radius of disk

 for i = 1:n

    theta = rand(1,n)*(2*pi);
    rs = sqrt(rand(1,n))*dradius;
    x = rs.*cos(theta);
    y = rs.*sin(theta);

end

xsim = x;
ysim = y;
% %plot (x,y,'.')
```

```matlab
%Step #3 multiply the poissonian distribution of numbers
%to the random airy disk points to solve for emmission points
%pattern of photon emission will be correlated with pattern of emission
%doubly stochastic

for i = 1:n
%     (sqrt(x(i).^2 + y(i).^2)) <= dradius;
        x1(i) = k1(i).*(x(i)); % multiplying random numbers by a 0 or 1
        y1(i) = k1(i).*(y(i)); % multiplying random numbers by a 0 or 1
%     (sqrt(x(i).^2 + y(i).^2)) > dradius;
end


for i = 1:n


    if x1(i) == 0 && y1(i) == 0;
        z1(i) = 0;


    else
        z1(i) = 2; %assume all emmission point are 2 units away from
dish vertex
    end
end

%Step #4 designate a 3xn emission points
x2=x1; % keeping same x position as from emission
y2=y1; % keeping same y position as from emission
z2 = z1';
emissionptsxyz = horzcat(x1,y1,z2);% designate 3xn emission points



%Step #5 Allocate emission points with a ray that intersects
%a triangular surface mesh defined with ptcloudtomesh.m file.
%The output files of ptcloudtomesh are in a structure with variable
%matricies:%
%                         vertices: Nx3 vertex coordinates
%                         triangles: M triangles using index numbers of
the vertices
%                         resolution: the mean edge length of triangles
%                         stdeviation: the standard deviation o edge
lengths
%                         triangleNormals: Mx3 normal vectors of each
triangle
%                         vertexNormals: Nx3 normal vectors of each
vertex
%                         vertexNtriangles: Nx1 cell of neighboring
triangles
%                                     of each vertex
%                         triangleNtriangles: Mx1 cell of nieghboring
triangles
%                                     of each triangle
%
%and using raytriangleintersect.m find the triangle that a specific ray
intersects than
%allocate a scalar multiplication to the ray to define the ray length
```

91

```matlab
%from the emission point to the triangulated surface. Use the unit
normal
%from the triangular surface to get the reflected ray direction.
%emissionptsxyz(all(emissionptsxyz==0,2),:)=[];
    scalar = ones(n,1); %using a nx1 of value one to test my scalar
about should be 0 or value other than 1
    d = [0 0 -1]; %Direction of ray vector
    k = size(triangles,1);  %Size of triangles matrix
    trinorm = zeros(n,3); % initialize trinorm vector
    refptxyz = zeros(n,3); % initialize refptxyz vector

for i = 1:n
    if emissionptsxyz(i,3) == 0;
        %o(i,1:3) = [0 0 0];
        scalar(i) = 0;
        continue;
    else %emissionptsxyz(i,3) == 2;  %for non zero emission points pick
which triangle it hits
            o = emissionptsxyz(i,1:3);%origin for raytriint ray
            for j = 1:k
            trivert(j,:) = triangles(j,1:3);
            p0 = vertices(trivert(j,1),1:3);
            p1 = vertices(trivert(j,2),1:3);
            p2 = vertices(trivert(j,3),1:3);
        [flag, u, v, t] = rayTriangleIntersection(o, d, p0, p1, p2);
%call function and pass variables
            if flag
                scalar(i) = t;%scalar value t is listed as variable
scalar after ran through code
                trinorm(i,1:3) = triangleNormals(j,1:3);
                break
            end
            end
    end
end
%Calculate arrival times
%reflectoray
incvecxyz = [0,0,-1];
for i = 1:n
    if scalar(i) == 0;

        refrayin(i) = 0;
        refnormray(i,:) = [0,0,0];
        %refnormray = horzcat(x6(i)',y6',z6');
    elseif scalar(i) ~= 0;

        refrayin(i) = (2.*(dot(trinorm(i,:),incvecxyz))); %inner
product
        refrayout(i,:) = refrayin(i)*trinorm(i,:);
        refnormray(i,:) = incvecxyz - refrayout(i,:); %total reflected
normal unit ray

    end
end

%detector
```

```matlab
% define a position vector for the detector and an orientation
% the detector is at a focal length of 1.3 units from the vertex
% of the parabola, the detector will be a square with radius 0.02 unit
% by 0.02 units
detorient = [0,0,-1];
detorienttrans = detorient';
detcent(1:3) = [0, 0, 0.65];
%detcent = horzcat(x5,y5,pz5); %location vector of detector from
parabola vertex
detcenttrans = detcent';
%detbound = (+/- 0.02(x) +/- 0.02(y), 0(z))

% Solve for a scale factor (a) to multiply to the reflected ray to
reach the
% detector surface

for i = 1:n
    if scalar(i) == 0;
    dethit(i,:) = [0,0,0];


    elseif scalar(i) ~= 0;
    refptxyz(i,:) = [emissionptsxyz(i,1:2),(2 - scalar(i))];

    paradetdis(i,:) = detcent(1:3) - refptxyz(i,:);%distance between
parab and det
    anumerator(i) = dot(detorient,paradetdis(i,:)); % a numerator
    adenominator(i) = dot(detorient,refnormray(i,:)); % a denominator
    a(i) = anumerator(i)/adenominator(i); %total scalar multiplier for
refraynorm
    detvect(i,:) = (a(i)*refnormray(i,:));
    dethit(i,:) = (detvect(i,:))+ refptxyz(i,:); %surface hit location?

    % if abs(dethit(:,1) | abs(dethit(:,2) > 0.02;
    % toa(i)


    end
end
%scatter3(refptxyz(:,1),refptxyz(:,2),refptxyz(:,3),'.');
plot(dethit(:,1),dethit(:,2),'.');
axis([-2,2,-2,2])
title('Detector Plane Photon Hit')
xlabel('Meters')
ylabel('Meters')
hold on;

%photontimes
%generate emission times incrimented by avt for n times
for i = 1:n

    % if abs(dethit(:,1) | abs(dethit(:,2) > 0.02;
    % toa(i) = 0;
    % else
    dist1(i) = sqrt(sum(abs(emissionptsxyz(i,:) - refptxyz(i,:)).^2));
    dist2(i) = sqrt(sum(abs(refptxyz(i,:) - dethit(i,:)).^2));
```

```matlab
        totdis(i) = dist1(i)+dist2(i);
        toa(i) = totdis(i)./299792458;


    end


    for i = 1:n


        if toa(i) > 0
            toaphot(i) = 1;
        else
            toaphot(i) = 0;
        end


    end


avt = 5e-11;
%avt = 6.67e-9;
for i = 1:n
    photemtimes(i) = avt *(i); %incremental times
end


%generate total photon arrival times.  Allocate a k2(i) to be 1 and 0's
%for arrival photons
for i = 1:n


    if k1(i) == 1 % & toa(i) > 0
        totalphtoa(i) = photemtimes(i) + toa(i);
        k2(i) = 1;


    else if k1(i) == 0
            totalphtoa(i) = 0;
            k2(i) = 0;
        end
    end
end


%photonarrivaltimes
for i = 1:n
    photonemmission(i) = ((photemtimes(i)+(8.8394485523e-9)))*k1(i);
%added time of 2.65m /c
end


photemtimes1 = (photonemmission');
 totalphtoa1 = (totalphtoa');%*1e10);
%  pois1 = horzcat(photemtimes,k4);
%  pois2 = horzcat(totalphtoa,k2);
 x_spikes = (photemtimes1(find(photemtimes1))');
 y_spikes = (totalphtoa1(find(totalphtoa1))');
```

pointCloud2mesh.m [40]

```matlab
function mesh = pointCloud2mesh(data)%, refNormal, stdTol)

% mesh = meshD(data, refNormal, stdTol)

% Author : Ajmal Saeed Mian {ajmal@csse.uwa.edu.au}
%           Computer Science. Univ of Western Australia
%
% This function takes data points performs triangulation on it, filters
out
% incorrecp polygons and outputs a mesh data structure like the newMesh
% function.
%
% Arguments : data - Nx3 vertex coordinates [x y z] of the pointcloud
%             stdTol - (optional) tolerance for edge filtering. default
is 0.6
%
%             refNormal - (optional) 1x3 vector in the sensor direction
%                        =[0 0 1] if the sensor looking towards the -
z_axis
%
% Return : mesh - mesh data structure
%                          vertices: Nx3 vertex coordinates
%                          triangles: M triangles using index numbers of
the vertices
%                          resolution: the mean edge length of triangles
%                          stdeviation: the standard deviation o edge
lengths
%                          triangleNormals: Mx3 normal vectors of each
triangle
%                          vertexNormals: Nx3 normal vectors of each
vertex
%                          vertexNtriangles: Nx1 cell of neighboring
triangles
%                                   of each vertex
%                          triangleNtriangles: Mx1 cell of nieghboring
triangles
%                                      of each triangle
%
warning off MATLAB:divideByZero;
if nargin == 1
    PC = princomp(data);
    data = data*PC;
    refNormal = [0 0 1];
    refNormal = refNormal * PC;
end

if nargin < 3
    stdTol = 3;
end

tri = delaunay(data(:,1),data(:,2));
tri(:,4) = 0; % initialize 4th column to store maximum edge length
```

95

```matlab
edgeLength = [sqrt(sum((data(tri(:,1),:) - data(tri(:,2),:)).^2,2)),...
        sqrt(sum((data(tri(:,2),:) - data(tri(:,3),:)).^2,2)),...
        sqrt(sum((data(tri(:,3),:) - data(tri(:,1),:)).^2,2))];

tri(:,4) = max(edgeLength,[],2);

resolution = mean(edgeLength(:));
stdeviation = std(edgeLength(:));
filtLimit = resolution + stdTol*stdeviation;

bigTriangles = find(tri(:,4) > filtLimit); %find index numbers of
triagles with edgelength more than filtLimit
tri(bigTriangles,:) = []; % remove all triangles with edgelength more
than filtlimit
tri(:,4) = []; % remove the max edgeLength column

edgeLength(bigTriangles,:) = []; % remove edges belonging to triangles
which are removed
edgeLength = edgeLength(:);
resolution = mean(edgeLength); % find the mean of the remaining edges
stdeviation = std(edgeLength);

mesh = [];
if nargin < 2
    data = data*PC';% multiply the data points by the inverse PC
    refNormal = refNormal * PC';
end
mesh.vertices = data;
mesh.triangles = tri;
mesh.resolution = resolution;
mesh.stdeviation = stdeviation;

noOfpolygons = size(tri,1);
noOfpoints = size(data,1);
mesh.triangleNormals = zeros(noOfpolygons,3); % innitialize a matrix to
store polygon normals
mesh.vertexNormals = zeros(noOfpoints,3); % innitialize a matrix to
store point normals
mesh.vertexNtriangles = cell(noOfpoints, 1); %a cell array to store
neighbouring polygons for the current point
mesh.triangleNtriangles = cell(noOfpolygons, 1); % to store neighbors
of current polygon

for ii = 1:noOfpolygons %find normals of all polygons
    %indices of the points from which the polygon is made
    pointIndex1 = mesh.triangles(ii,1);
    pointIndex2 = mesh.triangles(ii,2);
    pointIndex3 = mesh.triangles(ii,3);

    %coordinates of the points
    point1 = mesh.vertices(pointIndex1,:);
    point2 = mesh.vertices(pointIndex2,:);
    point3 = mesh.vertices(pointIndex3,:);

    vector1 = point2 - point1;
```

```matlab
    vector2 = point3 - point2;

    normal = cross(vector1,vector2);
    normal = normal / norm(normal);

    theta = acos(dot(refNormal, normal));
    if theta > pi/2
        normal = normal * (-1);%pointing down -1 pointing up 1
        a = mesh.triangles(ii,2);
        mesh.triangles(ii,2) = mesh.triangles(ii,1);
        mesh.triangles(ii,1) = a;
    end

    mesh.triangleNormals(ii,:)=normal;

    %make entry of this polygon as the neighbouring polygon of the
three
    %vertex points

mesh.vertexNtriangles(pointIndex1,1)={[mesh.vertexNtriangles{pointIndex
1,1} ii]};

mesh.vertexNtriangles(pointIndex2,1)={[mesh.vertexNtriangles{pointIndex
2,1} ii]};

mesh.vertexNtriangles(pointIndex3,1)={[mesh.vertexNtriangles{pointIndex
3,1} ii]};
end

for ii = 1:noOfpoints %find normals of all points
    polys = mesh.vertexNtriangles{ii};% get neighboring polygons to
this point
    normal2 = zeros(1,3);

    for jj = 1 : size(polys,1)
        normal2 = normal2 + mesh.triangleNormals(polys(jj),:);
    end

    normal2 = normal2 / norm(normal2);
    mesh.vertexNormals(ii,:) = normal2;
end

for ii = 1 : noOfpolygons % find neighbouring polygons of all polygons
    polNeighbor = [];
    for jj = 1 : 3
        polNeighbor = [polNeighbor
mesh.vertexNtriangles{mesh.triangles(ii,jj)}];
    end
    polNeighbor = unique(polNeighbor);
    polNeighbor = setdiff(polNeighbor, [ii]);
    mesh.triangleNtriangles(ii,1)={[polNeighbor]};
end
```

rayTriangleIntersection.m

```matlab
function [flag, u, v, t] = rayTriangleIntersection(o, d, p0, p1, p2)
%Ray/triangle intersection
%Input :
% o : origin
% d : direction
% po,p1,p2: vertices of the triangle
% trinorm: normal vector of triangle face
% Output:
% flag: (0) Reject, (1) Intersect
% u,v: barycentric coordinates
% t: distance from the ray origin
epsilon = 0.00001;
%Find vectors for two edges sharing p0
e1 = p1-p0;
e2 = p2-p0;
q = cross(d,e2); %begin calculating determinant
a = dot(e1,q); %determinant of the matrix M

if (a>-epsilon && a<epsilon)  % the vector is parallel to the plane
(the intersection is at infinity)
    [flag, u,  v, t] = deal(0,0,0,0);
    return;

end;


f = 1/a;   %inverse of determinant
s = o-p0; %vector from origin to first vertice
u = f*dot(s,q); %Barycentric parameter

if (u<0.0 || u>1.0)
    %the intersection is outside the triangle
    [flag, u,  v, t] = deal(0,0,0,0);
    return;
end;

r = cross(s,e1);
v = f*dot(d,r);

if (v<0.0 || u+v>1.0)
    %the intersection is outside the triangle
    [flag, u,  v, t] = deal(0,0,0,0);
    return;
end;

if (v >= 0.0 && u >= 0.0 && u+v <= 1.0)% is the condition of inside
    t = f*dot(e2,r);
    flag = 1;
    %tnm(j,1:3) = triangleNormals(j,1:3);
    return;
end
```

Correlation Calculation

```
tdiv = 500; %time bins
n1av = hist(x_spikes,tdiv);
n2av = hist(y_spikes,tdiv);
d = zeros(1,tdiv);
d1 = 0;
d2 = 0;
for i= 1:tdiv
d(i) = (n1av(i)*n2av(i));
d1 = d1 + n1av(i)^2;
d2 = d2 + n2av(i)^2;
end
d3 = (sum(d));
d4 = sqrt(d1*d2);
correlation = d3/d4;
```